

Fabrication and characterization of triple cation mixed halide perovskite solar cells using MACl_x



Mahnoor Mirza

00000203161

A thesis submitted in partial fulfillment of requirements

For the Degree of Master of Science in

Physics

Supervised by:

Dr. Faheem Amin

Co-Supervised by:

Dr. Muhammad Sultan (NCP)

Department of Physics
School of Natural Sciences
National University of Science and Technology
H-12, Islamabad, Pakistan
2020


National University of Sciences & Technology**MS THESIS WORK**

We hereby recommend that the dissertation prepared under our supervision by: Mahnoor Mirza, Regn No. 00000203161 Titled: Fabrication and characterization of triple cation mixed halide perovskite solar cells using MAClx Be Accepted in partial fulfillment of the requirements for the award of **MS** degree.

Examination Committee Members

1. Name: DR. FAHAD AZAD Signature: 

2. Name: DR. SYED RIZWAN HUSSAIN Signature: 

External Examiner: DR. ZULQARNAIN ALI Signature: 

Supervisor's Name: DR. FAHEEM AMIN Signature: 

Co-Supervisor's Name: DR. M. SULTAN Signature: 


Head of Department

09/09/2020
Date

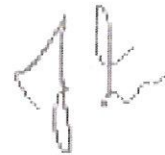
COUNTERSIGNED

Date: 09/09/2020


Dean/Principal

THESIS ACCEPTANCE CERTIFICATE

Certified that final copy of MS thesis written by Mahnoor Mirza (Registration No. 00000203161), of School of Natural Sciences has been vetted by undersigned, found complete in all respects as per NUST statutes/regulations, is free of plagiarism, errors, and mistakes and is accepted as partial fulfillment for award of MS/M.Phil degree. It is further certified that necessary amendments as pointed out by GEC members and external examiner of the scholar have also been incorporated in the said thesis.



Signature: _____

Name of Supervisor: Dr. Faheem Amin

Date: 09-09-2020

Signature (HoD): _____

Date: 9/9/2020

Signature (Dean/Principal): _____

Date: 09-9-2020

*Dedicated to my beloved parents,
Mr. and Mrs. Kazim Mirza
Who taught me to trust in ALLAH
and believe in hardwork.
Their prayers, love, strength and
motivation made me what I am
today!*

Acknowledgments

All praise to the gracious, the most merciful Almighty ALLAH, who has given me the courage, strength, opportunity and His blessings to complete my research. Without ALLAH's assistance this achievement would not have been possible.

*I owe my deepest gratitude to my supervisor, mentor **Dr. Faheem Amin** for his guidance, recommendations, boundless help and support throughout this work. His ultimate effort, attention and valuable suggestions helped me complete this research.*

*I would like to thank my co-supervisor **Dr. Muhammad Sultan** from NCP for his significant direction and support all over my research. I am very obliged to the principal of SNS **Dr. Rashid Farooq** and HOD of Physics **Dr. Shahid Iqbal** for their valuable guidance and suggestions. A special thanks to my GEC members, **Dr. Fahad Azad** and **Dr. Syed Rizwan Hussain** for their assistance, insightful comments and encouragement.*

*I am highly thankful to the Key laboratory of materials for energy conversion and storage of Shanxi province, Shanxi University China. I would like to express my deepest acknowledgments to **Prof. Gaoyi Han** and **Wenjing Hou** for allowing me to work in their labs and for their genuine and unconditional support in lab work.*

*A very special group of friends to mentioned here, because they deserve their own part. I would like to thank all my righteous friends **Ruttab Nadeem**, **Sundus Gul**, **Saira Parveen**, **Sadaf Fatima** for their love, motivation and prayers. It is a pleasure to thank them for their friendship, support and for the splendid time we shared. I am grateful to **Afsheen Zahra** for helping me and making things easier for me.*

*Last but not the least always comes my family, my deepest appreciation goes to my loving **parents**, sister **Shazil Kazim**, brother **Zeeshan Mirza** for their prayers, inspiration and moral support throughout my study.*

Mahnoor Mirza

Abstract

Perovskite solar cell (PSC) is a modern competitor within a photovoltaic research community. The power conversion efficiency (PCE) of a PSC has extended from 3.8% to above 22%, which interprets one of the fastest growths in a PV community. Perovskite as a light-harvesting layer has captivating photonic and electrical properties like long diffusion length, high absorption coefficient, low bandgap, less defect density and less excitons binding energy. Considering these properties, perovskite have become an outstanding choice for thin-film solar cells. Bandgap tunability of PSC makes them interesting with other established solar cell technologies.

Planar PSC with mixed cations and halide perovskite were prepared which reveals better performance in contrast with single cation/halide perovskite. In addition, bandgap of a perovskite material can be tuned by incorporating mixed cations/halides into single cation/halide perovskite. Mixed cations (MA, FA, Cs) with mixed anions (Br, Cl, I) was used with different concentrations of MAI (0, 0.025, 0.05, 0.07M/L). MAI helps in the crystal nucleation process. MAI_{0.025} exhibits a highest PCE of 16.4%. Perovskite with this concentration produced large grain size and reduce the pinholes. Overall PSC performance varies between MAI_{0.025} and MAI_{0.05}. Moreover, device without encapsulation under a dark environment with controlled relative humidity could still maintain 71% of the original PCE after six days.

Table of Contents

Chapter 1	1
Introduction:	1
1.1 Photovoltaic's.....	1
1.2 Perovskite solar cells:	2
1.2.1 Perovskite materials:	3
1.2.2 Charge Transport Absorbing layers:.....	5
1.2.2.1 Electron Transport Layer:.....	5
1.2.2.2 Hole Transport Layer:.....	6
1.2.3 Device architecture and mechanism of PSCs:.....	6
1.3 Various device architectures of PSCs:.....	7
1.3.1 N-i-p mesoscopic PSC:.....	7
1.3.2 P-i-n mesoscopic PSC:	8
1.3.3 N-i-p planar PSC:	8
1.3.4 P-i-n inverted PSC:	8
1.4 Properties of good solar absorber:	9
1.4.1 Bandgap:	9
1.4.2 Ferroelectric behavior:.....	10
1.4.3 Optical absorption:	10
1.4.4 Carrier diffusion length:	10
1.5 Solution based Fabrication Techniques:	11
1.5.1 One-step Deposition Technique:	11
1.5.2 Two-step Deposition Technique:	12
1.6 Challenges:	13
1.6.1 Stability:	13
1.6.2 Toxicity:	14
1.6.3 J-V Hysteresis:	14
1.7 Motivation:.....	15
1.8 Objective:	15

Chapter 2	17
Literature Survey.....	17
2.1 Origin of PSCs:.....	17
2.2 Previous study on PSC:.....	19
2.3 Shockley Queisser Limit Theory:	26
2.4 Function of selective contacts:	27
2.4.1 Transparent electrode:	27
2.4.2 HTM:.....	28
2.4.3 ETM:	28
2.4.4 Perovskite material:	29
2.4.5 Metal electrode:	30
Chapter 3	31
3.1 Experimental:.....	31
3.1.1 Apparatus:.....	31
3.1.2 Cleaning of substrates:.....	32
3.1.3 Synthesis of Charge transport Materials:	32
3.1.3.1 Electron transport material:	32
3.1.3.2 Perovskite Materials:	33
3.1.3.3 Hole Transport material:.....	33
3.1.4 Fabrication:	33
3.2 Deposition techniques:	35
3.2.1 Spin coating:.....	35
3.2.2 Thermal evaporation:	36
3.3 Characterization Techniques:	37
3.3.1 XRD:.....	37
➤ Measurement of crystals size:	38
➤ Bragg's Law:	38
3.3.2 SEM:	40
➤ EDS:	42
3.3.3 UV-VIS Spectroscopy:.....	43
➤ Working principle:	43
➤ Beer Lambert's Law:.....	44
➤ Tauc Plot Method:.....	45
3.3.4 Current voltage characteristics:.....	45

Chapter 4	48
Results and Discussion:	48
4.1 Sample detail:	48
4.2 X-Ray Diffraction (XRD):	48
4.3 Scanning Electron Microscopy (SEM):	49
4.4 UV-VIS Spectroscopy:	50
4.4.1 UV-VIS of Perovskite layer:	51
4.4.2 Bandgap of Perovskite Material:	51
4.5 J-V measurements:	52
4.5.1 J-V curves:	52
4.5.2 Stability Curves:	53
Chapter 5	55
Conclusion:	55
5.1 References:	57

List of Tables

Table 1: Background review of perovskites.....	18
Table 2: Summary of previous and recent reported PCSs.....	19
Table 3: Sample detail.....	48
Table 4: Summarized photovoltaic parameters with PCE.....	53

List of Figures

Figure 1.1: Categories of solar cell.....2

Figure 1.2: Efficiencies reached for third-generation thin-film cells as claimed by a latest NREL PCE report3

Figure 1.3: ABX_3 perovskite structure consists of A position (organic cation), B position (metal cation) and X position (halide anion)4

Figure 1.4: Diagrammatic representation of general layered PSC.....7

Figure 1.5: Representation of mesoscopic and planar devices i) mesoscopic n-i-p ii) mesoscopic p-i-n iii) planar n-i-p iv) inverted p-i-n.....9

Figure 1.6: Schematic of One-step deposition technique.....12

Figure 1.7: Schematic of Two-step deposition technique.....13

Figure 1.8: J-V characteristics a) Low hysteresis b) High hysteresis15

Figure 2.1: Demonstrated efficiencies with their bandgaps for a third-generation PV technology in contrast with S-Q limit27

Figure 3.1: Review of fabrication process.....31

Figure 3.2: Two-step deposition method.....34

Figure 3.3: a) Device architecture (n-i-p) b) Perovskite layer coated film c) Fabricated PSC device.....34

Figure 3.4: Spin coater.....35

Figure 3.5: Thermal evaporator.....37

Figure 3.6: General schematic of Bragg’s law39

Figure 3.7: Bruker D8 Advance X-ray Diffractometer.....40

Figure 3.8: Diagrammatic representation of SEM41

Figure 3.9: FE-SEM Apparatus.....42

Figure 3.10: Uv-visible spectrophotometer (Agilent 8453).....	43
Figure 3.11: Working representation of UV-Visible spectroscopy.....	44
Figure 3.12: CH1660D electrochemical workstation with solar simulator.....	46
Figure 3.13: Representation of I-V curve.....	47
Figure 4.1: XRD pattern of the perovskite layer of four samples.....	49
Figure 4.2: SEM images of four samples with a magnitude of X20,000.....	50
Figure 4.3: Uv-visible spectra o four samples.....	51
Figure 4.4: Bandgaps of four samples.....	52
Figure 4.5: J-V curves of PSCs.....	53
Figure 4.6: Stability curves of PSC.....	54
Figure 4.7: PSC with normalized PCEs.....	54

List of Abbreviations

PV: Photovoltaic

PSC: Perovskite solar cell

OSC: Organic solar cell

DSSC: Dye-sensitized solar cell

QDSC: Quantum dot solar cell

ETM: Electron transport material

ETL: Electron transport layer

HTM: Hole transport material

HTL: Hole transport layer

V_{oc} : Open-circuit voltage

I_{sc} : Short circuit current

J_{sc} : Current density

FF: Fill factor

PCE: Power conversion efficiency

XRD: X-ray diffraction

SEM: Scanning electron microscopy

UVO: Ultraviolet Ozone

AM1.5: Air Mass radiation at the surface of earth

FTO: Fluorine-doped tin oxide

ITO: Indium tin oxide

MAPbI₃: Methylammonium lead iodide

MACl: Methylammonium chloride

MABr: Methylammonium bromide

MAI: Methylammonium iodide

FAI: Formamidinium iodide

PbI₂: Lead iodide

CsI: Cesium iodide

SnO₂: Tin oxide

Spiro-MeOTAD: 2,2',7,7'-Tetrakis[N,N-di(4-methoxyphenyl)amino]-9,9'-spirobifluorene

Li-TFSI: Lithium bis(trifluoromethanesulfonyl)imide

TBP: Tributyl phosphate

Ag: Silver

IPA: Isopropyl alcohol

DMF: N,N-Dimethyl formamide

DMSO: Dimethyl sulfoxide

DI: De-ionized water

Chapter 1

Introduction:

In the twenty-first century, energy shortage has become a worldwide challenge. Presently, the major cause of energy generation in a world is fossil fuel. But because of the utilization of fossil fuels, energy crisis has been grown. Due to this reason, the development of renewable energy technology (e.g. hydroelectric, wind, geothermal and solar technology) has gained much attention in the replacement of energy generation based on fossil fuels. The most favourable technology is the solar energy to meet expanding world-wide energy challenges.

In this chapter, a brief introduction of photovoltaic and perovskite solar cell is given. The architectures of PSC their mechanism, categories, fabrication techniques, properties of light-harvesting layer and the current issues in PSCs are also discussed.

1.1 Photovoltaic's:

Basically, it is a process which converts light into electricity, called photovoltaic effect. Alexandre Edmond Becquerel (French physicists) first distinguished the PV effect in 1839. In 1954, Bell laboratories in U.S. demonstrated the first solar PV device that generates a utilizable amount of electricity. A photovoltaic absorber material is necessary for any solar cell, which not only absorbs the incoming light but also creates electron, holes and mobile charge carriers that are split at the interface of a device without any considerable loss of energy [1]. Photovoltaic based solar cells with a dominance of fragmentation and feasibility have gained remarkable consideration in a past half century. Major types of photovoltaic cells include Polycrystalline, mono-crystalline and thin films. Figure 1.1 categorizes the types of solar cell which classifies into first, second and third-generation cells.

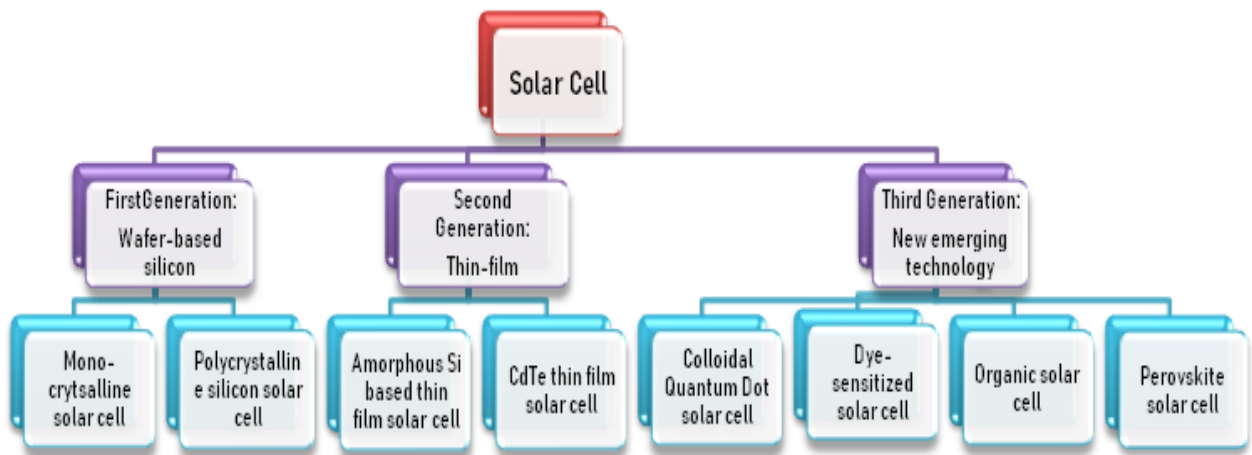


Figure 1.1: Categories of solar cell

Recently, solar cells based on crystalline silicon have control in a photovoltaic trade. However, a new emerging solar cell named as Perovskite solar cells have receive much concentration as a developing substitute of the silicon photovoltaic devices because of its large throughput and cost-valuable material, with a record efficiency of around 26% [2].

1.2 Perovskite solar cells:

Organic, in-organic PSCs have engaged significant consideration in a research area of solar cell because of its unbelievable power conversion efficiency (PCE) enhancement from 3.8% published by Miyasaka and coworkers in 2009 [3] to 22.1% till 2016 [4]. Present state-of-the-art PSCs achieved the PCE of 24.2% with its continuous progress in the field [5]. The highest PCE of PSCs is about 31% according to the theoretical calculations [6]. Figure 1.2 shows the record efficiencies attained over time for different third-generation technologies, where perovskite shows the highest efficiency [7]. As research pursued, efficiencies of various technologies are likely to continue growing.

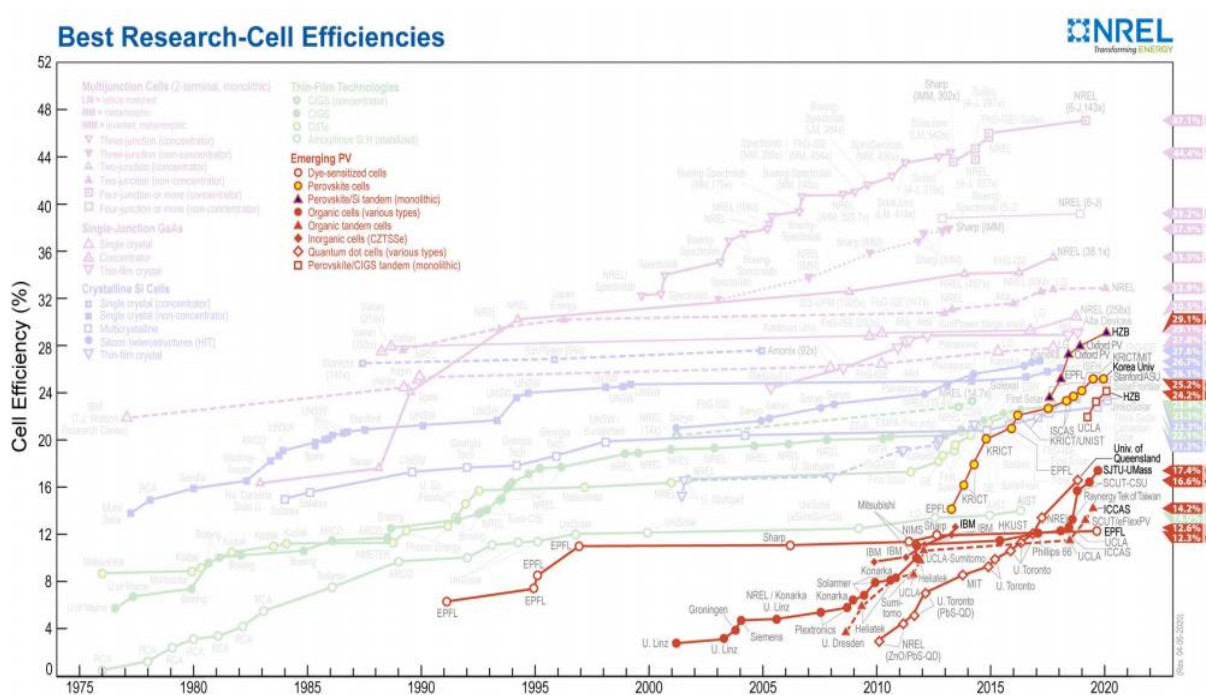


Figure 0 : Efficiencies reached for third-generation thin-film cells as claimed by a latest NREL PCE report [7]

1.2.1 Perovskite materials:

Perovskite material refers to a crystal structure having basic formula ABX_3 appeared in Figure 1.3 [8]. A perovskite material has a crystal structure following $CaTiO_3$ configuration. In a crystal structure ABX_3 , A denotes the organic or inorganic cation which is (MA^+) Methylammonium $CH_3NH_3^+$, (FA^+) Formamidinium $NH_2CH=NH_2^+$ and Cesium (Cs^+) . B shows the in-organic cation i.e. Pb^{2+} or Sn^{2+} while X shows the halide anion i.e. I, Cl⁻ and Br⁻. B and X forms an octahedral network where B and X are located at the core and apex of the octahedral respectively and A cation is surrounded by an octahedral network. Additional anion on a unit cell faces shows a best structure of a perovskite which is same as bcc. The most common perovskite materials are $MAPbI_3$, $MAPbBr_3$. There are some beneficial properties of these perovskite materials which include low bandgap, which limits the highest achievable PCE according to the (S-Q) Shockley-Queisser limit, they have high charge carrier mobility due to which electron and holes easily move through the material, they also have a high diffusion length which avoids the recombination.

Based on the chemical formula ABX_3 and ionic radii (r_i), perovskite structure's stability is prevised by using Goldschmidt Tolerance Factor (t). It is a proven implication to indicate about structure formation [9]. It is calculated by using the expression:

$$t = \frac{r_A + r_X}{1.41 (r_B + r_X)}$$

Here, r_A = radius of A cation

r_B = radius of B cation

r_X = radius of X anion

Generally, when t is 1, perovskite contains a cubic structure and when $0.8 < t < 1$, perovskite gives best stabilized structure. As the t increases, value of symmetry also rises due to which bandgap reduces [10].

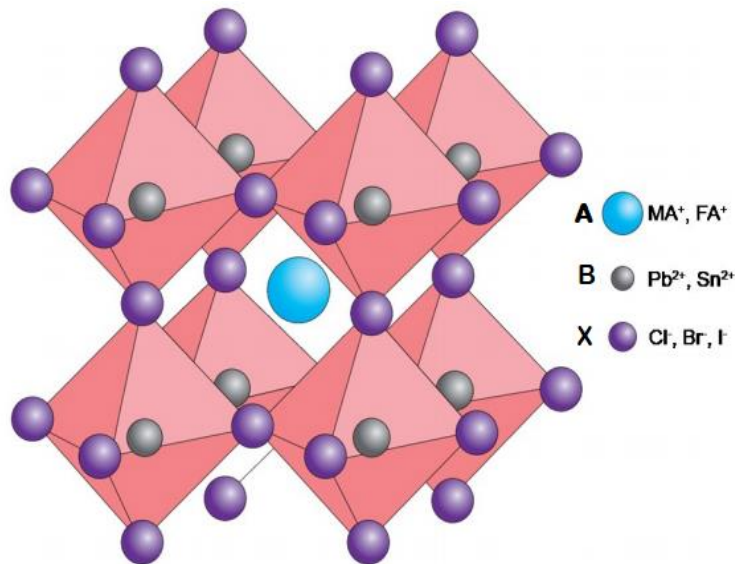


Figure 1.3: ABX₃ perovskite structure consists of A position (organic cation), B position (metal cation) and X position (halide anion) [8]

There are different materials which can be used as a perovskite absorber layer which includes; i) Methylammonium lead iodide (MAPbI₃): It exhibits excellent electrical and optical properties with a promising bandgap of 1.55eV. It has become one of the most favorable perovskite absorbers. ii) Methyl ammonium lead tribromide (MAPbBr₃): In the development of the perovskite layer, bromide is playing a role in replacement of iodine. It gives high bandgap of 2.3eV than iodide perovskites and exhibits distinctive properties. However, this perovskite has low optical absorption, but it gives large open-circuit voltage

compared to the iodide perovskite due to bromide presence. iii) Mixed halide perovskites: it consists of $\text{MAPb}(\text{I}_{1-x}\text{Cl}_x)_3$, $\text{MAPb}(\text{I}_{1-x}\text{Br}_x)_3$, $\text{MAPbI}_{3-x}\text{Cl}_x$ etc. Both of perovskite $\text{MAPbI}_{3-x}\text{Cl}_x$ and MAPbI_3 have direct bandgaps of 1.5-1.6eV and have a high absorption coefficient. Generally, these halide perovskites are helpful in increasing stability, bandgap tuning and also boost charge transport [11].

1.2.2 Charge Transport Absorbing layers:

A charge transport operation in PSCs is affected by the order of energy level among the active layer and electrode's work function. By adding a narrow charge carrier layers between an electrode and absorption layer, order of energy level can be tuned. These layers are a limiting aspect of the efficiency of PSCs. Transport layers having low mobility can increase the recombination. To counteraction this phenomenon, two tactics can be used: doping in the transport layer and using the materials having high mobility. But doping might result in some issues like diffusion of dopant, degradation etc. So, to attain the high efficiency, careful electron and hole transport layers should be selected.

1.2.2.1 Electron Transport Layer:

To attain a large open-circuit voltage (V_{oc}) and good fill factor (FF) in the PSC, a lot of effort needed in scheming the nanostructures which are influential as ETM. Larger electron mobility is essential for ETLs. The most common ETMs are ZnO, SnO_2 and TiO_2 with high efficiency and good FF. TiO_2 have a large bandgap of 3.02eV. Its valence band edge is lying at a low level due to this it is a good hole blocking layer [12]. Mesoporous structure, tube-shaped nanostructures can be formed by TiO_2 . It is considered as an ideal ETM for the sake of its excellent properties like large mobility, best environmental stability and acceptable energy level. ZnO have also larger bandgap of 3.3eV and it exhibits 60meV excitons binding energy at RT. The ionization potential of ZnO is high so it acts as an HTL because of its larger bandgap. SnO_2 have a larger bandgap as well, larger intrinsic electron mobility, and higher transparency which makes it dominant as an ETM. Some other materials like PCBM, CuAlO_2 are used as an ETM. ETL is the important layer in PSC for device stability and performance.

1.2.2.2 Hole Transport Layer:

In general, HTL is important in PSC because it transfers the light-induced holes within the perovskite to an opposing electrode. To achieve a best efficiency effort are in progress on using best HTMs. The high hole mobility is required for HTM. A most commonly used organic HTM is spiro-MeOTAD. Due to its good ionization potential and large solubility, currently, this is a best HTM used in excessive efficiency PSCs. But it also has some defects like its high cost, low hole mobility and low conductivity which causes interfacial recombination losses. It needs dopant to improve the FF, hole conductivity and PCE. Other organic HTMs like P3HT, PEDOT:PSS and DEH are used as an HTL. By blending P3HT with carbon nanotubes as a HTL had attained a PCE 15% with outstanding long term stability [13]. Some inorganic HTMs like nickel oxide (NiO_x), Copper thiocyanate (CuSCN), Copper iodide (CuI), Molybdenum oxide (MoO_3), Tungsten trioxide (WO_3), Vanadium pentaoxide (V_2O_5) is used as an HTL in PSCs.

1.2.3 Device architecture and mechanism of PSCs:

PSC's general layer structure is represented in figure 1.4, which comprises a transparent electrode which may be FTO or ITO, hole transport layer (HTL), perovskite absorber layer, electron transport layer (ETL) and metal electrode. Architecture of PSCs also originates from a DSSC type architecture [14]. In that case, perovskite absorber layer was used as "dye" molecules but perovskite was not a firm "dye" because it dissolves quickly in the liquid HTL and its PCE was about 3.8% [14]. Another research used the same structure but with thinner TiO_2 layer, so the efficiency arises to 6.5%. A perovskite shows good absorption of light as compared to dye molecules [15]. Basic solar cell working operation includes; i) photon absorption ii) creation of excitons iii) detachment of charges iv) transfer of charges v) collection of charges. When light falls, photons are absorbed in a light-harvesting layer and it creates excitons. The unbound charge carriers diffuse as well as drift due to the electric field, so the electrons are shifted to (ETM) electron transport material and holes are shifted to (HTM) hole transport material. Then transparent electrode collects the electrons and the back metallic electrode collects the holes. Eventually, photocurrent is induced in an outer circuit by connecting a transparent and metal electrode.

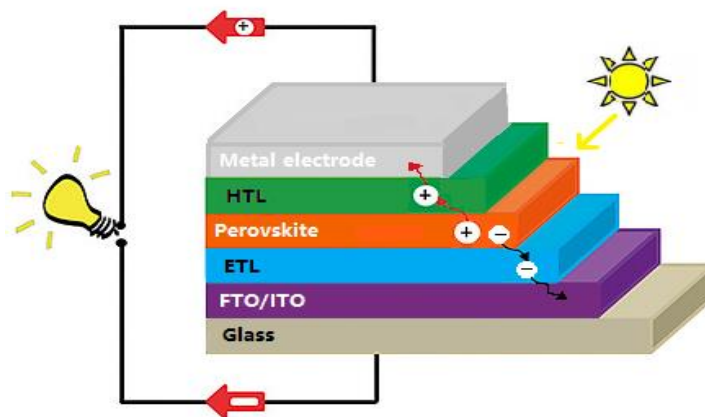


Figure 1.4: Diagrammatic representation of general layered PSC

1.3 Various device architectures of PSCs:

PSCs are further divided into four classes; i) n-i-p mesoporous ii) n-i-p planar iii) p-i-n mesoporous iv) p-i-n planar presents in figure 1.5 [16]. Researchers also studied about ETL-free and HTL-free structures. Mesoporous structure was first used in DSSCs as a sensitizer. For this structure, usually, TiO_2 is deposited as a compact ETL and above this layer, mesoporous ETL (generally TiO_2 , Al_2O_3 , Au@TiO_2 , BaSnO_3) [17-20], as a metal oxide scaffold is assembled at high temperature $>400^\circ\text{C}$ by sintering the tiny particles together. The remaining layered structure is like the general perovskite structure. Mesoporous material helps to increase the light-collecting region of photosensitive material and improves a device PCE. The other advantage of the mesoporous device is having shorter electron diffusion length as compared to the planar device structure [21]. It is easy to fabricate the mesoporous films than the planar films and for the perovskite devices; these are the main reason for the cost advantage. To cope with the charge transportation and recombination process, interface engineering of mesoscopic materials is helpful. In planar device structure, sintering at high temperature is not required. Planar structure eliminates the porous metal oxide scaffolding; this is the main difference from mesoporous device structure. The absence of this porous oxide layer results in a simple planar structure. But perovskite absorbing layer should be controlled carefully [22].

1.3.1 N-i-p mesoscopic PSC:

An ideal mesoscopic n-i-p configuration has revealed a PCE 21.6% since 2016 [23]. In n-i-p mesoporous, transparent electrode/ETL/mesoporous scaffold/perovskite/HTL/metal electrode

is the device structure shown in figure 1.5(i) where, ETL works as a n-type, mesoporous scaffold with perovskite works as an i-type and HTL works as p-type.

1.3.2 P-i-n mesoscopic PSC:

For p-i-n, device architectures are reversed like transparent electrode/HTL/mesoporous scaffold/perovskite/ETL/metal electrode (figure 1.5(ii)).

1.3.3 N-i-p planar PSC:

In planar PSC, electron-hole pairs are separated more quickly by ETL and HTL respectively after light absorption in an absorbing layer [24]. Planar structure n-i-p consists of transparent conductive electrode/ETL/perovskite/HTL/metal electrode (figure 1.5(iii)). In this structure ETL is n-type, perovskite is i-type and HTL is p-type. Planar n-i-p PSC has exhibited highest efficiency 20.7% since 2016 [25]. For planar structure, usually TiO_2 , SnO_2 , ZnO are used as an ETL, Spiro-MeOTAD used as a HTL [26]. As the perovskite film growth needs a hydrophilic surface and organic transport layer i.e. Spiro-MeOTAD cannot help in the film's growth. It is a challenge for the growth of transport layer film to deposit TiO_2 , ZnO or PEDOT: PSS because either it uses high temperature which is the reason of decomposition of perovskite film or it uses such solvents which may dissolve the perovskite film [27]. Generally, the most favored ETL is TiO_2 , but as an ETL ZnO have superior properties as compared to the TiO_2 . Also, perovskite which uses ZnO as an ETL decomposes at a higher rate compared to TiO_2 perovskite cells [28].

1.3.4 P-i-n inverted PSC:

Inverted configuration originates from (OSCs) organic solar cells [29]. ETL and HTL layers are reversed in this structure. Inverted p-i-n has exhibited PCE 18% [30]. It contains transparent electrode/HTL/perovskite layer/ETL/metal electrode shown in a figure 1.5(iv). HTL works as a p-type, perovskite layer is i-type and ETL works as an n-type. In this architecture, mostly PEDOT: PSS, NiO_x used as an HTL and ZnO , PCBM/BCP, PCBM is used as an ETL. Many state-of-the-art perovskite materials like FAPbI_3 , MAPbI_3 and MAPbBr_3 are used as a perovskite absorber layer and metal electrodes like Silver, Gold, Aluminum is used in PSCs [26].

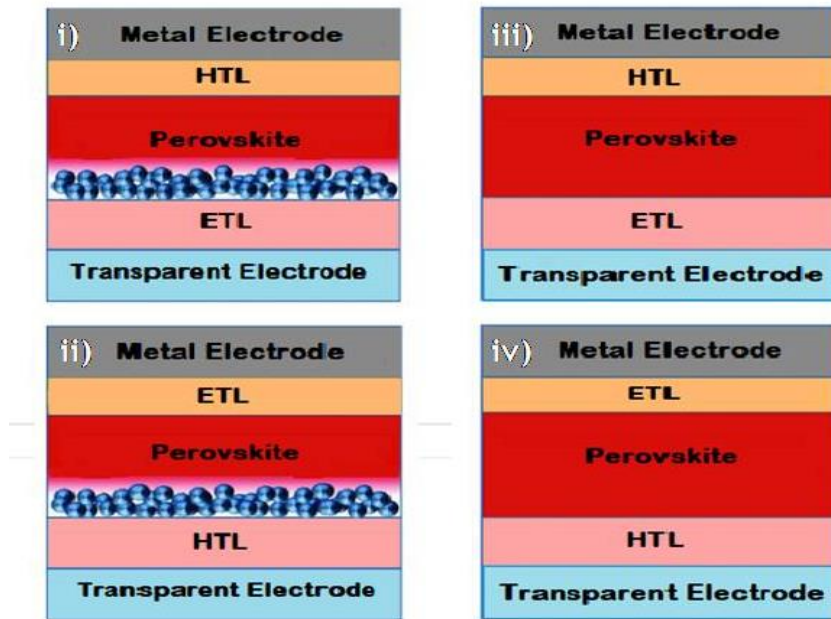


Figure 1.5: Representation of mesoscopic and planar devices i) mesoscopic n-i-p ii) mesoscopic p-i-n iii) planar n-i-p iv) inverted p-i-n

1.4 Properties of good solar absorber:

There are some fundamental properties of a light-harvesting layer that helps in improving device efficiency.

1.4.1 Bandgap:

Bandgap is the most significant property of perovskite absorber. Maximum theoretical efficiency can be determined by the help of bandgap. Bandgap has a direct impact on device performance. Bandgap ranges from 1.1-1.5eV have the best device efficiency. 1.34eV is the ideal bandgap which also satisfies Shockley Queisser limit. In some cases, bandgap tuning is needed so that it can extend shorter absorption to the larger absorption wavelength without loss of its absorption coefficient. One way to tune the bandgap is, changing MA by other organic cations. Bandgap can be tuned by the A site (organic cations) of ABX_3 since they improve the bond length M-X-M and angle without any influence on maximum valence band. Some mixed halide perovskite like bromide and chloride [31] , iodide and bromide [32] has a tuneable bandgap.

1.4.2 Ferroelectric behavior:

Ferroelectric feature gives a feasible route to separate charge carriers by exhibiting spontaneous polarization. This bulk PV effect causes PCE of the device exceeding the S-Q limit. Some ferroelectric materials have a large bandgap like for lead zirconate titanate ($\text{Pb}[\text{Zr}_x\text{Ti}_{1-x}]\text{O}_3$) E_g is greater than 3.5eV and for bismuth ferrite (BiFeO_3) E_g is greater than 2.8eV. If the bandgap of a ferroelectric perovskite is decreased polarization is also decreased. Bandgap can also be reduced by considering chalcogenide ferroelectric materials. There are some advantages of ferroelectric behavior such that restricts electron hole pair recombination and charge screening with a high degree. If ferroelectric materials have a large dielectric constant it validates lesser defects binding energies which develop shallow defect states. So, the ferroelectric behavior is the main feature for hysteresis as well.

1.4.3 Optical absorption:

Optical absorption is a key parameter which helps in developing high efficiency of the device. Perovskite has high optical absorption than silicon solar cell and it helps in avoiding transmission losses. As all the PV devices reveals some obvious absorption threshold. Electricity conversion may not take place if the energy of entering photons is less as compared to the threshold. High optical absorption is attained in the direct bandgap materials. As the absorption is high, absorber layer is thinner which is advantageous for device efficiency. Materials having an absorption coefficient with an optical bandgap and high efficiency are more favorable candidates for solar cells.

1.4.4 Carrier diffusion length:

Light-induced carriers has a diffusion length which is the most fundamental feature associated to the optoelectronic device performance. This can be enhanced by improving the film morphology. For good device performance, grain size is the primary parameter that should be optimized. Diffusion length should be greater than the thickness of perovskite layer. If perovskite layer's thickness is greater than the diffusion length, as produced carriers will recombine before getting to the ETL. For the greater light-induced carrier diffusion length which is greater than $1\mu\text{m}$, the main reason is less concentration of carrier traps and the non-radioactive recombination centre [33]. Incorporating halogen elements at X sites have various advantages like it improves the stability of the material, high mobility, carrier transport, and carrier diffusion length.

1.5 Solution based Fabrication Techniques:

1.5.1 One-step Deposition Technique:

This method is commonly utilized in the synthesis of perovskite material because of its easier operation. It needs a minimum step to synthesize the perovskite layer. For one-step method, mixture of $\text{CH}_3\text{NH}_3\text{X}$ and PbX_2 where, $\text{X}=\text{Br}, \text{I}, \text{Cl}$ dissolved in a solvent [17]. This precursor solution was deposited on a substrate as shown in figure 1.6 [34]. After spinning, annealing is done which turns the yellowish film to blackish. The annealing temperature is important for the fine crystallization of perovskite film because the lower temperature leads to the poor film while the higher temperatures result in the active layer's decomposition [35]. Usually, the solvents (DMF) dimethylformamide, (DMSO) dimethyl sulfoxide and (GBL) gamma-butyrolactone reported for solution processes. The mixture of GBL and DMF gives a best results due to which fast vaporization of this solvent combination occurred [36]. Various deposition techniques can be used like Spin coating, Drop-casting, Doctor Blade, Slot-die coating, ultrasonic spray coating, Electrodeposition etc. The widely used technique is spin coating. It is important to control perovskite precursors with pinhole-free and appropriate stoichiometry. In most cases, there are voids on the perovskite layers in the result of one-step deposition which is the reason for faster recombination. It is difficult to control fast crystal growth during annealing in this method because crystal growth has low energetic barrier. So, the pinholes and uncovered perovskite film is the reason for poor performance and non-ideal reproducibility.

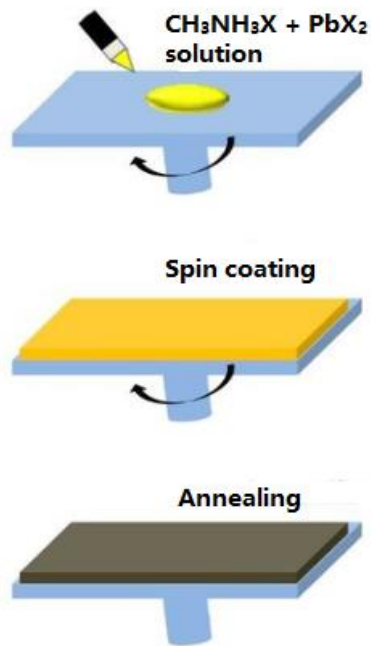


Figure 0Schematic of One-step deposition technique

1.5.2 Two-step Deposition Technique:

Two-step deposition technique uses separate layer growth of both CH₃NH₃X and PbX₂. Three ways are possible for this method; Spin coating, Vapour assisted deposition, Dipping. In case of spin coating, start with spin coat PbX₂ solution on the substrate and after that, CH₃NH₃X is spun on the PbX₂ layer and after annealing results in perovskite thin film as shown in figure 1.7 [34]. For vapour assisted deposition CH₃NH₃X is vapour deposited on to the PbX₂ coated film and for dipping, PbX₂ coated film is immersed into the CH₃NH₃X solution. This method produces uniform and defect-free layers. This technique results in better morphology and reproducibility compared to the one-step technique. But the chances of environmental changes and human error are greater in this method.

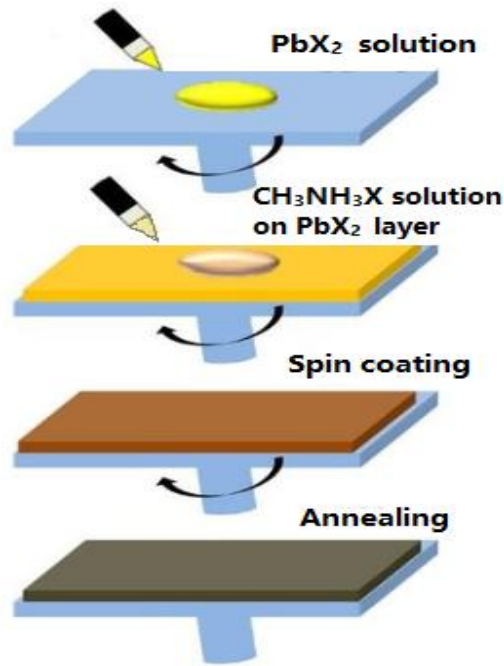


Figure 1.7: Diagrammatic Representation of Two-step deposition technique

1.6 Challenges:

PSCs have some challenges which should be overcome to become more dominant. These challenges include stability, Toxicity, J-V Hysteresis. All the below-given challenges need to be resolved, before proper utilizing PSC technology.

1.6.1 Stability:

Stability of the solar cell is a crucial challenge especially when it encounters the normal environmental conditions. There are some main causes of instability in PSCs which includes;

- TiO_2 as an ETL, under UV illumination it gives rise to the photocatalytic degradation. To improve stability, TiO_2 can be replaced with some other UV- stable materials like BaSnO_3 [37] or by adding an interfacial modifier like Sb_2S_3 , CsBr [38, 39] between the ETL and absorber layer.
- Most common used organic HTMs like Spiro-MeOTAD, P3HT and PTAA is the other reason for instability. In their doped forms, they experienced thermal or moisture instability. To resolve this issue, organic HTM can be replaced with inorganic materials, buffer layers can be inserted between perovskite and HTL.
- Metal electrodes like gold, silver and aluminum have also stability issues. Due to ion migration in perovskite, electrodes Ag, Al encounters corrosion which leads to change

of color and PCE reduction. Although Au diffuses over the organic HTL with a temperature more than 70°C which results in poor performance. To improve the stability, interfacial layers like Cr, MoOx, and RGO have been introduced to stop metal diffusion.

As by reported work on a stability evaluation, it should be enhanced in a perovskite photovoltaic industry. When PSC exposed to oxygen, humidity, ultraviolet radiations and temperatures, degradation in these cells occur. Encapsulation techniques also prove effective for the moisture sensitivity of PSCs. Niu et al. reported the chemical reactions due to which degradation of $\text{CH}_3\text{NH}_3\text{PbI}_3$ occur [40]. One year is the longest lifetime which is reported for PSCs [41] which is too less than the 25 years as required in the PV industry. So, the shortest lifetime is the prime barrier restricting the PSC photovoltaic in PV industry.

1.6.2 Toxicity:

This is another main challenge which needs to be resolved. The presence of lead in the perovskite layer is considered toxic because lead is hazardous to environment. It needs proper safety precautions. The good performance of PSC is with Pb atoms till now, whose commercialization is confined due to its toxicity. Sn can be replaced for Pb due to its less toxic nature. But Sn-based perovskite has very low efficiencies because when Sn based PSC exposed to air, fast oxidation in Sn occurs. To prevent the fast degradation Sn perovskite had to be carried out in nitrogen atmosphere. Halide PSC based on Sn have been reported which involve CsSnI_3 , $\text{CH}_3\text{NH}_3\text{SnI}_3$ and $\text{HC}(\text{NH}_2)_2\text{SnI}_3$. However, the highest PCE of these PSCs based on $\text{CH}_3\text{NH}_3\text{SnI}_3$, $\text{HC}(\text{NH}_2)_2\text{SnI}_3$ is about 9% [42]. To avoid the environmental contamination from Pb, Pb-free PSC are probably next extensively researched area for perovskite solar cells. Other than this drawback of Sn halide perovskite, it provides number of properties like narrow bandgap, high charge mobilities and binding energies which make them interesting for use in PV.

1.6.3 J-V Hysteresis:

When taking the J-V measurements of PSCs J-V scan parameters can be a factor which affects the desired results. If irregular J-V characteristics are the result of J-V scan, it presents the hysteresis which influences the measured PCE of the curve. Figure 1.8 demonstrates the hysteresis effect of J-V curves. (a) Shows the low hysteresis and (b) shows the greater hysteresis. Hysteresis effect is clearer in PSCs having defects which behave like a trap for electrons and holes. If the hysteresis is less, it means the perovskite layer is more uniform.

Hysteresis effect occurs due to many factors like ferroelectricity, ion migration and charge trapping [43]. Another cause which enhances the hysteresis effect could be high charge carrier mobilities, due to this I-V curve can be sensitive [44]. It is clear from the literature that films achieved by using ultrasonic spray coating technique having less hysteric effect as compared to that of conventional spray coating and spin coating. Planar PSC and Al₂O₃ based PSC has shown the highest hysteresis effect of about 50%, although TiO₂ based PSC has shown low hysteresis effect of about 15% [43]. Hysteresis effect can be controlled with the larger crystals and grain size which shows low liability to indicate hysteresis. So this is another challenge for PSCs in the PV community which was not discussed in detail until 2014 [43].

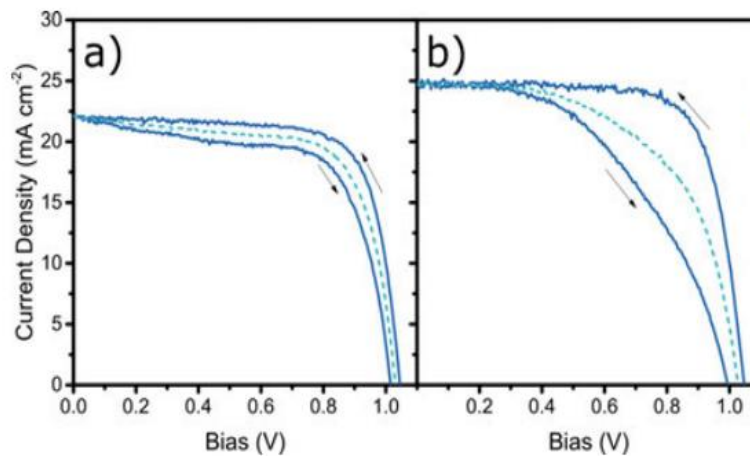


Figure 1.8: J-V characteristics a) Low hysteresis b) High hysteresis [45]

1.7 Motivation:

Solar energy is used to produce electricity through photovoltaic PV effect. It is a favorable technology which can remove the restricted proportion of fossil fuels. A type of photovoltaic, PSCs are appearing as the most optimistic solar cells with a highest efficiency of more than 22%. There is an outstanding development in research on PSC materials in the past some years.

1.8 Objective:

The central purpose of a thesis is to examine and characterize the mixed cations-halide perovskites. The objective of the study is to gather a better understanding of some basic manufacturing steps to attain high PCE and stability. Organic PSC has been fabricated via

easy techniques like thermal evaporation and spin coating to investigate parameters for fabrication and testing of the device.

Thesis Outline

Chapter # 1

- Brief introduction of PSC, its structure and challenges in PSCs

Chapter # 2

- Literature survey of history and recent progress in PSCs

Chapter # 3

- Fabrication of the device and their characterization techniques

Chapter # 4

- Results and discussion based on experimental work

Chapter # 5

- Conclusion

Chapter 2

Literature Survey

Origin of perovskite solar cells, the previous and recent study in PSCs is discussed in the given chapter. The role of layers deposited to fabricate a PSC is also explained.

2.1 Origin of PSCs:

Gustav Rose (German scientist) found calcium titanate (CaTiO_3) mineral from mountains during his trip to Russia in 1839. This mineral was named as “perovskite” in a prestige of Russian mineralogist Lev Perovski [46]. In 1892, H.L. Wells et al. synthesized first halide perovskite-based on lead and caesium. But its structure was determined by C.K. Moller at Denmark in 1950's which shows this is a perovskite structure. After the early discovery, it would be approximately half century before research began on perovskite materials. In that time, researchers studied the properties of perovskites which shows light emitting, superconductivity, thermoelectric, ferromagnetism, piezoelectricity and solar activity. Some other researchers at Western Electric (New York) and Philips (Netherland) innovates perovskite oxides. These oxides used in electromechanical transducers and condensers.

First organic-inorganic halide perovskite was developed by D. Weber at Germany in 1978 as briefly explained in the table 1. He replaced methylammonium ions to the caesium cations in the first halide perovskite by H.L. wells. After a long time of 16 years, light-emitting devices based on fluorescent organic-inorganic perovskite was developed by researchers at IBM T.J. Watson research centre, New York in 1994. After two years, Boeing North America (California) constructed a nonlinear optical crystal which was based on a caesium germanium halide salts for optoelectronics in 1996. In 1999, by using a rare earth-based perovskite compounds, manufacturing of an optical light harvesting layer for an SC was reported by M. Chikao et al. in Tokyo, Japan.

In the perovskite family, some other materials having high temperature superconductivity can be also discovered from them like $\text{YBa}_2\text{Cu}_3\text{O}_{7-\delta}$ (YBCO) and $\text{La}_{2-x}\text{Ba}_x\text{CuO}_4$. A keen evolution in a research area of PSCs taking it to the manufacturing methods, novel material formulations and its first steps to commercialization.

Table 1: Background review of perovskites

Year	Scientist / Organization	Discovery
1839	Gustav Rose (Germany)	He discovered CaTiO_3 type mineral from the Ural Mountains named as “perovskite”
1892	H.L. Wells, Sheffield scientific school (New haven, Connecticut)	Synthesized lead and caesium halide perovskites
1947	Philips (Eindhoven, Netherlands)	Discovers barium titanate BaTiO_3 which produces condensers.
1955	Western Electric (New York)	Used ferroelectric crystalline oxides for manufacturing of electromechanical transducers.
1957	C.K. Moller (Copenhagen, Denmark)	Analyze the structure of compounds produced by H.L. Wells.
1959	Clevite (Cleveland, Ohio)	Discovered perovskite materials in the manufacturing of piezoelectric resonators.
1962	A.E. Ringwood (Canberra, Australia)	Reported that Earth’s lower mantle is build from MgSiO_3 perovskite.
1975	Hitachi (Tokyo, Japan)	Produced gas sensors based on perovskite oxides.
1978	D. Weber (Stuttgart, Germany)	Fabricated the first halide organic-inorganic perovskites.
1981	GTE Laboratories (Waltham, Mass)	Innovated perovskite crystals based on lasers.
1988	Ferranti Plc (Oldham, U.K)	Discovered a perovskite structure having superconducting composition.
1994	IBM / D.B. Mitzi et al. (New York)	Developed fluorescent organic-inorganic perovskites.
1996	Boeing North America (California)	Developed caesium-germanium halide salts act as a nonlinear

		optical crystal.
1999	Murase Chikao et al. (Tokyo, Japan)	Constructed an absorption layer for a solar cell.

2.2 Previous study on PSC:

Previous study and recent progress on PSCs are reviewed in the Table 2. Perovskite materials, ETMs, HTMs and their deposition techniques are also shown.

Table 2: Summary of previous and recent reported PCSs

Perovskite Materials	Deposition Techniques	ETL	HTL	PCE %	Year	Ref.
MAPbI ₃ / MAPbBr ₃	Dropping	TiO ₂	I/I ₃	3.81	2009	[14]
MAPbI ₃	Spin coating	TiO ₂	I/I ₃	6.5	2011	[15]
MAPbI ₃	Spin coating	TiO ₂	No	5.5	2012	[47]
MAPbI ₃	Doctor blade/spin coating	TiO ₂	Spiro-MeOTAD	9.7	2012	[18]
MAPbI ₃	Spin coating	NR-TiO ₂	Spiro-MeOTAD	9.4	2013	[48]
MAPbI ₃	Spin coating	TiO ₂	Spiro-MeOTAD	2	2013	[49]
MAPbI ₃	Full printable	TiO ₂	CE	6.64	2013	[50]
MAPbI _n Br _{3-n}	Spin coating	TiO ₂	No	8.54	2014	[51]
FAPbI ₃	Spin coating	TiO ₂	Spiro-MeOTAD	14.2	2014	[52]
MAPbI ₃	Spin coating	PC61BM	NiO	9.51	2014	[53]
MAPbI ₃	Spin coating	TiO ₂	CuI	6.0	2014	[54]

MAPbI _{3-x} Cl _x	Spin coating	PCBM/ PFN	PEDOT:PSS	17.1	2014	[55]
MAPbI _{3-x} Cl _x	Spin coating	TiO ₂ /Al ₂ O ₃	Spiro-MeOTAD	13.3	2014	[56]
MAPbI ₃ /MAPbCl ₃	Spin coating	TiO ₂ /Zr O	Spiro-MeOTAD	15.8	2015	[57]
MAPbI ₃	Spin coating	ZnO	Spiro-MeOTAD	11	2015	[58]
FAI,PbI ₂ ,MABr,PbBr ₂	Spin coating	Nd doped TiO ₂	Spiro-MeOTAD	18.1	2015	[59]
MAPbI ₃	Spin coating	C ₆₀ /BCP	PCT	16.5	2016	[60]
MAPbI ₃	Spin coating	PCBM	NiO	18.2	2016	[61]
MASnPbI ₃	Spin coating	C ₆₀ /BCP	PEDOT:PSS	13.6	2016	[62]
MAFAPbI ₃	Spin coating	SnO ₂ /C ₆₀ SAM	CZ-TA	18.3	2017	[63]
MAPbI ₃	Spin coating	PCBM	PTPD/PFN	19.1	2017	[64]
(FAPbI ₃) _{1-x} (MAPbBr ₃) _x	Spin coating	SnO ₂	Spiro-MeOTAD	21.5	2017	[65]
CsPbI ₂ Br	Spin coating	ZnO/C ₆₀	NiO _x	13.3	2018	[66]
KI-doped (FAPbBr ₃) _{0.875} (CsPbBr ₃) _{0.125}	Spin coating	TiO ₂	Spiro-MeOTAD	18.5	2018	[67]
RbCsFAPbI ₃	Spin coating	SnO ₂	Spiro-MeOTAD	20.4	2018	[68]
MAPbI ₃	Thermal evaporation/S pin coating	C ₆₀ /BCP	PTAA	21.1	2019	[69]
PEAI/FA _{1-x} MA _x PbI ₃	Spin coating	SnO ₂	Spiro-MeOTAD	23.2	2019	[70]

G-S-CsPb _{0.6} Sn _{0.4} I ₃	Spin coating	PCBM/B CP	NiO _x	13.3	2019	[71]
MAPI	Thermal evaporation	C ₆₀ /BCP	TaTm/MoO ₃	18	2020	[72]

A very first PSC is manufactured by Miyasaka(2009) [14]. In this article he used TiO₂ as an ETL, iodide and bromide liquid electrolytes as an HTL and MAPbI₃, MAPbBr₃ perovskites. MAPbI₃ perovskites have slightly low V_{oc} of 0.61V and bromide perovskite gives V_{oc} of 0.96V. This high V_{oc} is due to the bromide because it has larger bandgap compared to the iodide. Iodide perovskite gives a high efficiency of 3.81% while the bromide perovskite has a low efficiency of 3.13% due to the shorter current density.

Two years later, perovskite QD sensitized solar cell was fabricated by an iodide liquid electrolyte and lead iodide perovskite, its processing was improved. Due to which efficiency is increased by 6.5% having a V_{oc} of 0.706V, FF is 0.58 and J_{sc} is 15.8mAcm⁻². But it had stability issue because of iodide electrolyte. Perovskite crystals decomposed in a liquid electrolyte due to which fast degradation occurs [15].

In 2012, Lioz Etgar and his coworkers reported HTL free PSC. Lead iodide perovskite with TiO₂ as an ETL was used. In this architecture, back electrode collects the holes due to the absence of HTL. Here, MAPbI₃ perovskite plays the role of both light absorption and hole conductor. This HTL free PSC reached the efficiency of 5.5% with a low V_{oc} of 0.63V, FF of 0.57 and J_{sc} of 16.1mAcm⁻² [47].

At the same time, other researchers have reported their work in which they replaced iodide liquid electrolyte with spiro-MeOTAD as an organic HTL; they attained PCE of 9.7% higher than the previous one. V_{oc} of 888mV, FF of 0.62 and J_{sc} of 17.6mAcm⁻² was attained with a high stability over 500hrs without encapsulation [18].

Hui-Seon Kim at al. discussed TiO₂ Nano-Rod sensitized solar cells with MAPbI₃ perovskites in 2013. TiO₂ Nanorods were prepared hydrothermally. By controlling the reaction time, length of nanorod varied. This solar cell attained a V_{oc} of 955mV, FF of 0.63 and J_{sc} of 15.6mAcm⁻² with the corresponding PCE of 9.4%. The device performance depends on a length of nanorod. As the NR-TiO₂ length increases, both V_{oc} and PCE decrease [48].

Another work with same lead perovskite but TiO_2 as an ETL has achieved PCE of 2% having V_{oc} of 0.645V, J_{sc} of 7mAcm^{-2} and FF of 0.445. The efficiency of device is very low due to its low fill factor [49]. Zhiliang Ku and his coworkers fabricated heterojunction solar cells with mesoscopic MAPbI_3 , TiO_2 as an ETM and Carbon counter electrode in the replacement of HTM through a full printable method. By using carbon electrode this PSC produced efficiency of 6.64% with a high stability of 840hrs [50].

Sigalit Aharon et al. reported HTL free PSC in 2014. They used $\text{MAPbI}_n\text{Br}_{3-n}$ for both absorbing and hole conductive layer. They studied different concentrations of iodide and bromide which shows that they can conduct holes in any composition. Two-step deposition technique is applied here which is also advantageous for bandgap tuning. PCE of 8.54% attained with corresponding J_{sc} of 16.2mAcm^{-2} , FF of 0.68 and V_{oc} of 0.77V. As the concentration of iodide and bromide changes efficiency is varied [51].

Eperon et al. discussed the influence of replacing MA cation with FA cation. They have used $\text{FAPbI}_y\text{Br}_{3-y}$, y varies from 0 to 1. Diffusion length measurements were also recorded for ideal device arrangement. They have achieved PCE of 14.2% due to high J_{sc} of 23mAcm^{-2} . A low bandgap of FAPbI_3 is the reason for a high current density [52].

Kuo-Chin Wang and his coworkers (2014) showed a little different PSC with Mesoscopic NiO as HTL and PC61BM as an ETL. Organic hole materials are replaced with a metal oxide which gives a strong device configuration for advance development of inorganic PSCs. These kinds of PSCs have attained a PCE=9.5%. The cell using PC61BM delivers a high V_{oc} of 1040mV, FF of 0.69 and J_{sc} of 13.24mAcm^{-2} [53].

In the same year, Christians et al. reported copper iodide (CuI) as an alternate of other HTMs. Compared to the other devices having Spiro-MeOTAD, V_{oc} is very low in this device. PCE of 6% has achieved with high stability [54].

Another group of researchers demonstrated moisture assisted film growth. They used PEDOT: PSS and PCBM as an HTL and ETL. They used another layer of PFN over PCBM which helps electron extraction from ETL to the Al (metal) electrode. This also enhances the FF and overall device performance. They have attained the efficiency of 17.1% with a high $V_{oc}=1.05$, $J_{sc}=20.3\text{mAcm}^{-2}$ and FF=0.80. This high V_{oc} and FF firmly show that recombination loss is reduced [55].

In another article, Daniel Bryant and his group demonstrated a semitransparent electrode configuration with transparent conducting contact adhesive (TCA). This device architecture is based on mesoscopic with $\text{TiO}_2/\text{Al}_2\text{O}_3$ as a compact ETL. It can be a low-cost good

alternative to Gold. It gives good conductivity, charge extraction and mechanical adhesion to the perovskite devices. 13.3% PCE is shown in this article with a $V_{oc}=0.95V$, $FF=63.6$ and $J_{sc}=20.7mAcm^{-2}$ [56].

In 2015, Hsin-Hua Wang and his group reported a quantitative and simplistic approach to enhance TiO_2 ETL in PSCs by incorporation of different acetylacetonate additives. Elements in the range of Zn (II), Y (III) and Zr (IV)-Mo (VI) was including in additives. For enhanced samples, J_{sc} was increased from 20-20.5 $mAcm^{-2}$, FF was increased from 0.75-0.765 and V_{oc} was increased from 1.009-1.025V. Regarding this, four additives demonstrate improved PCEs from 15.0-15.8%. Zr- TiO_2 based device gives the overall best device performance [57]. Jie Zhang et al. (2015) demonstrated synthesis of zinc oxide layers. These layers were composed of zinc nitrate precursor. Rapid, moderate-temperature and facile electrochemical method was used in the synthesis. The prepared layers were of good optical and structural quality. They reported about the low processing temperature which is adequate to fabricate PSCs. This layer was used as an efficient ETL with $MAPbI_3$ perovskites and Spiro-MeOTAD as an HTL which produces the PCE of 11% [58].

During the same year, Bart Roose et al. prepared mesoporous Nd-doped TiO_2 electrodes for PSCs. Three different concentration of Nd used (e.g. 0%, 0.3% and 0.5%). The best doping concentration is 0.3% which gives the PCE of 18.2% with a good V_{oc} and FF . This doping is beneficial for PSC because it helps in minimizing the charge recombination and also increases the electron transport in ETL; it also assists in improving device performance and stability [59].

In 2016, Weibo Yan et al. described the different conductive polymers that can be used as an HTL. They used $MAPbI_3$ perovskite with electron selective contact C_{60} and BCP as an ETL. Four different polymers such that i) (PCT) poly (3-chlorothiophene) ii) (PT) poly (thiophene) iii) (PMT) poly (3-methylthiophene) iv) (PBT) poly (3-bromothiophene) was used as an HTL. They were synthesized by the electrochemical polymerization process. As the work function of HTM is increased, V_{oc} also increased. In all of them, PCT shows overall good performance with the optimized best efficiency of 16.5% presenting a $V_{oc}=1.01V$, $FF=0.76$ and $J_{sc}=21.4mAcm^{-2}$ [60].

Yongzhen Wu and his group showed a fullerene heterojunction structure. This structure helps in reduction of recombination loss and enhances a collection of photoelectrons. Basically, their approach is to improve the inverted PSCs performance. They have attained a high PCE

of 18.21%. By controlling the energy levels of ETMs, HTMs and perovskite configurations, the performance of a device can exceed [61].

Yunlong Li and his coworkers (2016) reported about Sn-based PSC having an inverted planar architecture in which PEDOT: PSS used as an HTL, C₆₀ combine with BCP is used as an ETL and perovskite is MASn_{0.5}Pb_{0.5}I₃. This shows the uniform morphology of the film. Thickness and annealing temperature of a film was optimized. They have achieved a PCE=13.6% which representing this Sn-based PSC is the most efficient [62].

XinXing Yin et al. in 2017 used a carbazole-cored (CZ-TA) as an HTM which shows outstanding optoelectronic properties. SnO₂/C₆₀-SAM together used as an ETM and MA_{0.7}FA_{0.3}PbI₃ used as a light-harvesting layer. They found a maximum efficiency of 18.32% with CZ-TA HSL with a large FF=0.81, V_{oc}=1.044V and J_{sc}=21.66mAcm⁻² [63].

Compared to the Spiro-MeOTAD based device, it has also achieved PCE of 18.28% under the same condition. There is a little difference between both efficiencies. Jinho Lee and his group introduced a novel way of the interfacial manufacturing method. Hydrophobic HTLs was used which results in a scalable, full coverage and high-quality perovskite films. Seven different HTLs were used with an additional layer of PFN. This additional layer was used as an interfacial compatibilizer. By applying a PFN layer to the HTL, its surface polarity was improved which is also advantageous for enhancing perovskite coverage without influencing its electronic structure. This mechanism shows many advantages like its improved PCE, reproducibility, scalability and device stability. By using different HTLs, PTPD/PFN shows the highest PCE of 19.14% with the best FF, V_{oc} and J_{sc} of 0.81, 1.11 and 21.23mAcm⁻² respectively [64].

Another group of researchers in 2017, they used a two-step approach to synthesize a perovskite and to cope with PbI₂ quantity. They found that the excessive leftover of PbI₂ could be a reason of poor stability and hysteresis while the average leftover of PbI₂ can produce high efficiency and stability. There were some issues which influence the stability and the prime issue is the ion movement. It depends on PbI₂ residue. When the PbI₂ was insufficient, ion movement was stopped by FAI phase and when the vast crystallization of PbI₂ was high, ion movement could be easy. They have attained 21.6% of PCE by tuning the leftover of PbI₂ in small size area (0.073cm²) while PCE of 20.1% was delivered at large size area (1cm²) [65].

In 2018, Chong Liu et al. reported inorganic perovskite with NiO_x as an HTL and ZnO@C₆₀ as an ETL. They also discussed only C₆₀ as a layer which can be coated uniformly and creates the optimum interface between the perovskite and back electrode. It delivers low efficiency of 9.5% compared to the ZnO. The mobility of ZnO is more suitable than C₆₀. When ZnO incorporate with C₆₀ it delivers low leakage loss and large carrier extraction efficiency. This inorganic PSC gives the efficiency=13.3% with a high V_{oc}=1.14V, J_{sc}=15.2mAcm⁻² and FF=0.77. By thermal treatment at 85°C for 360hrs this inorganic PSC delivers 20% efficiency loss without encapsulation [66].

Dae-Yong Son et al. demonstrated the pure, mixed anion/cation halide perovskites with additional potassium iodide for better device performance. By adding a very minute quantity of (KI) potassium iodide can enhance the device performance and helps in the reduction of I-V hysteresis. Different trials with alkali metal iodides such that CsI, RbI, NaI and KI was performed which verified that the best element for this target is K ion. KI doping also decreased the low-frequency capacitance and trap densities. They called this method as a universal method to resolve the hysteresis issue in PSC. The maximum PCE of 18.56% was demonstrated by the 10μmol doping of KI in (FAPbBr₃)_{0.875}(CsPbBr₃)_{0.125} perovskite [67].

During 2018, Turren Cruz et al. fabricated an MA-free planar PSC which shows good stability high device performance. They used (Rb) rubidium and (Cs) Caesium instead of MA which gives highly crystalline optimized FA-based perovskites (RbCsFAPbI₃). They have an acceptable bandgap of 1.53eV which reached a higher efficiency=20.44% with a large J_{sc}=25.06mAcm⁻². This planar PSC was stabilized at 20.3% which is the most efficient among the highest MA free PSCs reported [68].

Zhaolai Chen et al. in 2019 reported an SC-MAPbI₃ (single crystal PSC) which attained a high efficiency of 21.09%. This PCE is the best among all the single-crystal PSCs. It produces the highest FF=0.83, V_{oc} =1.076V and J_{sc} =23.46mAcm⁻². This also helps in the reduction of I-V hysteresis which is almost negligible in this work. This best performance SC-PSC with a high FF and PCE features the assurance in PV technology [69].

Qi Jiang with his group showed the enhanced device performance by using (PEAI) phenethylammonium iodide salt as an additional on mixed perovskite to passivate a defective surface. It also prevents a non-radiative recombination and presents the best efficiency of 23.32%. At this point, the quasi-steady state is attained. Further they achieved high V_{oc} of 1.1.8V with a bandgap of 1.53eV. This bandgap is 94.4% of the S-Q limit V_{oc} [70].

Mingyu Hu and his coworkers (2019) revealed a low bandgap inorganic PSC which shows a long stability with interface functionalization. They used inorganic $\text{CsPb}_{0.6}\text{Sn}_{0.4}\text{I}_3$ perovskite revealing a bandgap of 1.38eV which satisfies an S-Q limit. Without any functionalization this perovskite shows a very low PCE of 0.92% after the (G-B) grain boundary functionalization it produces a PCE of 5.68% but this helps a uniform coating of the sample and also decreases the trap densities. For further enhancement surface functionalization was done over the (G-B) surface to make a Grain boundary surface functionalization. It upgrades the PCE to 13.37% which passivates the defective surface and reduce the degradation issues. This inverted planar PSC exhibits a lifetime of 1045hrs and long term stability [71].

Now in 2020, according to the recent report of Azin Babaei et al. vacuum-deposited inverted planar PSC was fabricated. They used TaTm combine with MoO_3 as a HTL and C_{60}/BCP used as an ETL. PCE of a device is increased from 16.5-18% at the annealing temperature of TaTm/ MoO_3 bilayers at 60 and 140°C respectively [72].

According to this literature survey, the highest efficiency reported in 2019 as 23.32%. It is also found that PSC is the birth of a new era in PV technology due to its high efficiency. However, some challenges should be resolved as soon as possible.

2.3 Shockley Queisser Limit Theory:

S-Q limit is described as a maximal power conversion efficiency of a cell that contains semiconducting absorber material with a bandgap E_g . It depends on a detailed balance principle which corresponds to a balance between the absorption and emission of light.

S-Q limit depends on a five-simple hypothesis:

- a) Thermalization of all the light-induced charge carriers to the band edges
- b) For every photon energy, the possibility for the light absorption in a PV absorber material is 1 if $E \geq E_g$ and 0 if $E < E_g$.
- c) At short circuit, the possibility of collection of light-induced carriers is 1.
- d) Collection of electrons and hole at their corresponding electrodes.
- e) Radiative recombination occurs by the photon emission.

Three different energy loss mechanisms can occur in S-Q model such that, optical, electrical and thermal energy loss. As stated by S-Q calculations, at the bandgap of 1.34eV the highest efficiency is around 33% using a solar cell (single junction). Although, many other this kind

of solar cells have demonstrated best efficiencies but lower than this PCE due to many factors which include surface defects, interfacial barriers and unpreventable impurities etc. As the bandgap moves from optimum $E_g=1.34\text{eV}$, the maximal limit of PCE reduces. Figure 2.1 shows the efficiencies with their bandgaps compared to the S-Q limit of different third-generation PV cells.

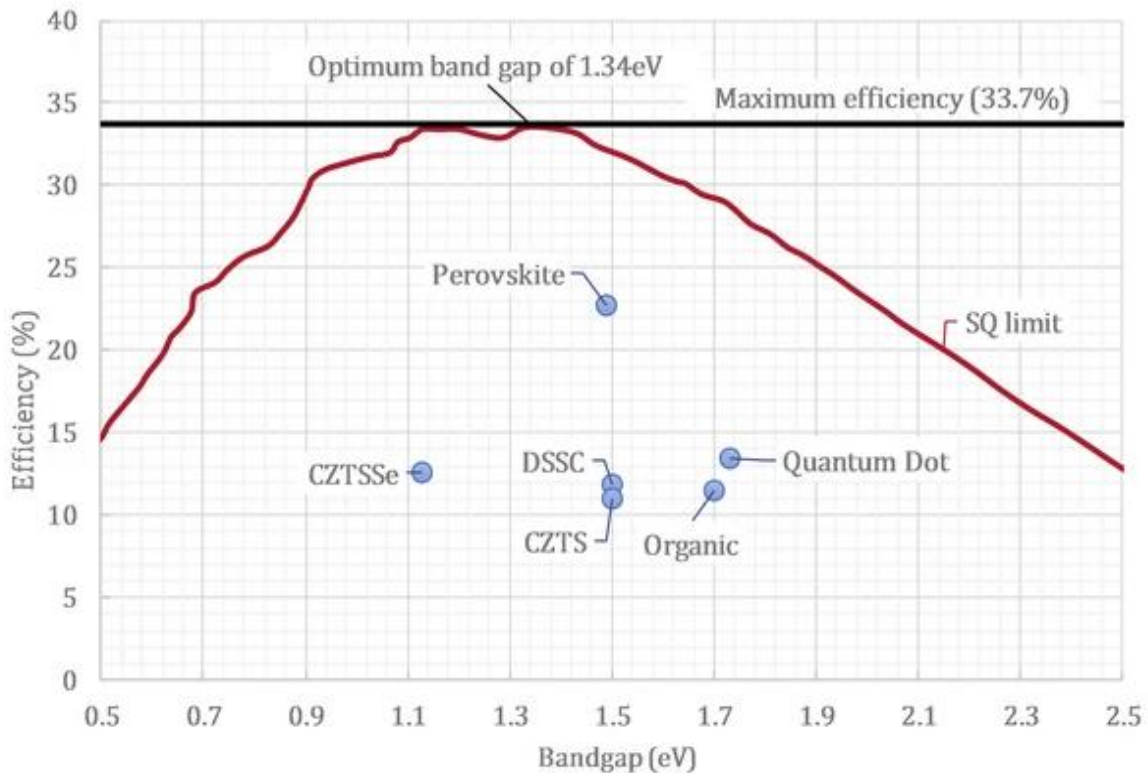


Figure 2.1: Demonstrated efficiencies with their bandgaps for a third-generation PV technology in contrast with S-Q limit [73]

2.4 Function of selective contacts:

2.4.1 Transparent electrode:

The transparent electrode is a thin film with an optical translucent and conductive material. ITO and FTO are more frequently used as a transparent electrode. It collects the electrons or holes and generates photo current. FTO electrode is used in this work. It has a large bandgap and its energy value is higher than the visible light. FTO is more conductive than ITO because at higher temperatures conductivity of ITO drops so FTO has good thermal stability.

2.4.2 HTM:

The major role of the HTMs in PSC is to accumulate and transfer the holes after a detachment of electron and holes in the light-harvesting layer. To accomplish a best performance PSCs, HTMs should fulfill the following conditions:

- a) High photochemical and hole mobility.
- b) For the highest photocurrent, absorption of light should be in near IR and visible part of a solar spectrum.
- c) Acceptable energy levels of HOMO coinciding with (VBE) valence band energy of perovskite materials, and also confirming the injection and transfers of holes.
- d) For the fabrication of the device, the potential of synthesizing a thin-film and the solubility of HTMs in organic solvents should be suitable.

FF depends on the HTM because the conductivity and series resistance of HTM strongly influences the FF. Photocurrent is also observed by the hole extraction rate of HTM. Organic HTM Spiro-MeOTAD is used in this work. Spiro and its derivatives in PSC devices have certified to be most favourable because it fulfills above-mentioned conditions. Doping of Li-TFSI and TBP is required in spiro-MeOTAD due to the deficit of π - π intermolecular force. After fabricating a device, Spiro-MeOTAD oxidation is needed to achieve a favourable HTM. Seok and his coworkers (2016) reported three composite pm, po and pp-spiroMeOTAD which reveals acceptable optical properties with high solubility and large bandgap [74]. A replaced derivative ortho-methoxy demonstrates a high LUMO level which helps in blocking of electrons and gives best FF with a high PCE. Generally, by replacing a methoxy group, LUMO and HOMO levels can be calibrated.

2.4.3 ETM:

ETL plays a remarkable role in a PSC performance. Generally, ETL makes an electron cautious contact with an absorption layer to enhance the electrons separation efficiency and blocking of holes. ETM should fulfill the following circumstances for the best performance PSC:

- a) Electron mobility should be high, so that electrons can transfer faster in the ETL.
- b) Optical transmittance should be high, which helps in lower the energy loss.
- c) The order of perovskite and ETM's energy level should be coincide for energetic charge transport and hole blocking.

- d) It should be simple processing and low cost to fabricate.

ETM must avoid recombination of holes at the transparent electrode interface. High mobility and a less free electron density both upgrade the J_{sc} and PCE of the devices. SnO_2 (tin oxide) is used in this work. SnO_2 in replacement of TiO_2 as an ETM in PSCs has produced broad interests. Both have same physical properties, crystal structures and energy level alignment. SnO_2 is observed as a optimistic substitute to TiO_2 because:

- a) It has a low temperature for the crystallization than TiO_2 , so it is very simple to doped and crystallize.
- b) It has high mobility i.e. $240\text{cm}^2\text{Vs}^{-1}$, due to which recombination losses are reduced and efficiency of electron transfer is enhanced compared to the other ETMs.
- c) It shows outstanding chemical stability, low photocatalytic activity, and good UV resistance which is good for device stability compared to the other ETMs.
- d) It has significant alignment of energy level at the perovskite and ETL interface.

SnO_2 have a broad bandgap of 3.5-4eV with a work function of 4.7-5.3eV. Qi Jiang et al. reported a highest efficiency of 23% by using SnO_2 as an ETM [70]. UVO treatment is useful for metal oxide surface development for better film quality. It eliminates the contaminants from the surface, decreases the oxygen vacancies and enhances the surface wettability. After the coating of SnO_2 on substrate, UVO treatment of few minutes is carried out to help better uniform coating of perovskite layer as reported in many literatures.

2.4.4 Perovskite material:

Perovskite layer transforms the UV and visible light into electricity very effectively. It involves the light-harvester absorbing materials which absorbs the photon and creates the excitons and then transfers an electrons and holes to their corresponding ETL and HTL. Electrons and holes can be efficiently transferring and collects. Their transfer distance is around 100nm or greater than $1\mu\text{m}$. For best performance perovskite layer, materials should have the following properties:

- a) Tuneable bandgap, in doped perovskite materials, bandgap can be tuned.
- b) Greater carrier mobility, which separates electron-hole pairs for excellent device performance
- c) Good optical absorption in a visible region

- d) Facile manufacturing because of high defect tolerance and low-temperature processing
- e) Large diffusion length and high carrier lifetime

In this thesis, mixed ions perovskite material which includes MAI, FAI, MABr, MACl, PBI₂ and CsI with two-step deposition approach is used. Bromide perovskite have broader bandgap than iodide which helps in increasing the open-circuit voltage. MACl causes phase change without annealing. Perovskite film quality can be enhanced by optimizing the MACl concentration. By tuning its quantity, grain size and phase crystallinity can be improved. These characteristics result in high V_{oc} and J_{sc} .

2.4.5 Metal electrode:

The top metal electrode collects the electrons or holes and produce current. Presently, gold is the most frequently used metal electrode used in PSCs which is quite expensive. Its alternative is silver which is low-cost, too cheaper than gold. Ag electrode is used in this work as a back electrode. These electrodes are also used to modify light management in PSC devices. Ag electrode has high conductivity and good optical transparency. But the only problem is degradation. Ag can decompose with a perovskite material and decreases the efficiency. From the air, gas molecules reach the perovskite materials and decompose in it producing iodine which diffuses in silver and makes silver iodide which degrades it easily. But this decomposition can be avoided by using a highly stable perovskite blend. Today, Au and Ag-based encapsulated PSC devices have shown good stability of up to 1000hrs and 500hrs under continuous illumination and under both heat and light conditions respectively [75].

Chapter 3

This chapter explains the cleaning of substrates, synthesis method of different layers like ETL, HTL, perovskite layer and fabrication of devices with four different concentrations of MAI. After the device fabrication, one of the important parameters is to test the devices. The deposition techniques which are used in the fabrication of solar cell are also explained. To check the morphology, absorption, chemical bonding and the structure of an active layer, different characterizations have been done.

3.1 Experimental:

In this section, cleaning of substrates, synthesis of ETL, HTL and perovskite layer is explained. Device fabrication is also described. Figure 3.1 briefly demonstrates the fabrication process.

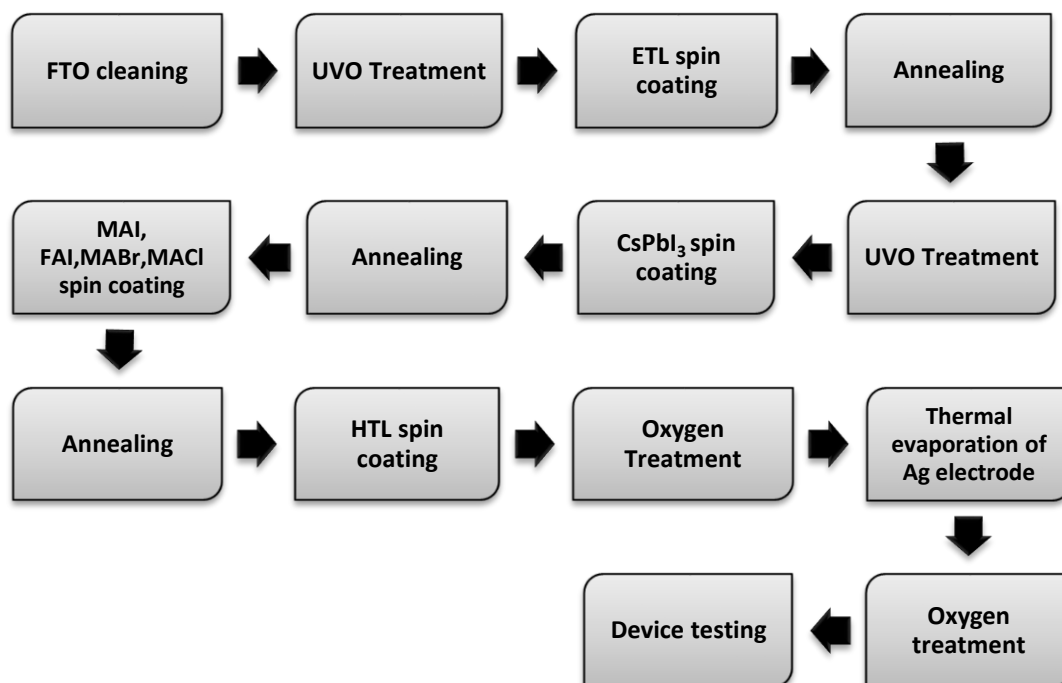


Figure 3.1: Review of fabrication process

3.1.1 Apparatus:

The apparatus used in the synthesis of materials and fabrication of devices is briefly introduced below:

- i. Substrate holder
- ii. Ultrasonic bath
- iii. Nitrogen gun
- iv. Oxygen gun
- v. UVO cleaner
- vi. Weight balance
- vii. Spin coater
- viii. Micropipette
- ix. Hot plate
- x. Beakers, Petri dish
- xi. Stirrers
- xii. Tweezers
- xiii. Syringe filter 0.2 μ m
- xiv. Shadow mask
- xv. Glove box

3.1.2 Cleaning of substrates:

FTO substrates (2.0 x 2.0cm) were bought from a Kunshan Sunlaite New energy technology, China. Substrates are required to clean before the deposition of layers. First, etched FTO substrates were put in a substrate holder and washed by using detergent, DI water, acetone and isopropanol (IPA) in a Sonicator for 30 minutes respectively. Contamination on the substrates can be removed by using cavitation bubbles induced from the high-frequency sound waves in an ultrasonic bath. After washing, each substrate was dried with the Nitrogen gun. Cleaned substrates were put in a UVO treatment for 45 minutes. Before the deposition of Electron transport layer, substrates were again cleaned by using a nitrogen gun.

3.1.3 Synthesis of Charge transport Materials:

3.1.3.1 Electron transport material:

Tin (IV) oxide, 15% in H₂O colloidal dispersion was purchased by Alfa Aesar. Dilute SnO₂ in Distilled water with the ratio of 1:5 respectively and sonicate for 15 minutes. This solution was deposited on the FTO substrate as an electron transport layer.

3.1.3.2 Perovskite Materials:

Lead (II) Iodide (PbI_2) 99.99% trace metal basis, perovskite grade and Cesium iodide (CsI) 99.9% trace metals basis, *N,N*-Dimethylformamide (DMF) 99.8% , Dimethyl sulfoxide $\geq 99.9\%$, Isopropyl alcohol (IPA) $\geq 99.7\%$ were purchased from Sigma Aldrich. Other chemicals Formamidinium iodide (FAI), Methylammonium iodide (MAI), Methylamine hydrochloride (MACl), Methylammonium bromide (MABr) with the highest purity was purchased from greatcellsolar materials. A mixture of PbI_2 and CsI was prepared by taking the molar ratio of 1.359M/L and dissolved in a DMF and DMSO with a ratio of 9:1 under stirring at 70°C for 12 hours. The other solution of MAI, MABr, FAI and MACl was prepared with four different concentrations of MACl with the constant values of the other three chemicals. Four concentrations of MACl was 0, 0.025, 0.05, 0.07M/L and the other three MAI, MABr, FAI with the molar ratio of 0.1195, 0.049 and 0.229M/L respectively was dissolved in 2ml of IPA under stirring for 30 minutes at room temperature. Perovskite materials were prepared under the glove box containing Helium gas.

3.1.3.3 Hole Transport material:

All precursors used in the synthesis of Spiro-MeOTAD were purchased from Sigma Aldrich. The solution of spiro-MeOTAD was prepared by taking 0.075g Spiro in 1000 μl Chlorobenzene followed by addition of 30 μl tert-butyl pyridine and Li-salt solution (0.013g Li-TFSI into 50 μl acetonitrile) under stirring at room temperature for 24 hours.

3.1.4 Fabrication:

As prepared SnO_2 solution (80 μl) as an electron transport layer was spin-coated on a cleaned FTO substrate at 3000rpm for 30 sec and annealed for 30 min at 150°C in air. After annealing, UVO treatment was carried out for 45 min to remove the contaminations and again cleaned by using Nitrogen gun. Perovskite solution was deposited using the two-step approach, first CsPbI_3 solution (65 μl) was spin-coated at 2300rpm for 30 sec and annealed for 1 min at 70°C . It gives yellow phase film, when it comes to the room temperature, then mixed organic cation-anion solution of MAI, MABr, FAI and MACl with four different concentrations (65 μl) was spin-coated at 2500rpm for 30 sec respectively on four devices in a glove box and annealed for 30 min at 150°C outside the glove box. Perovskite film immediately converts into the black after annealing. These layers react to make a perovskite layer. Figure 3.2 represents the two-step approach of fabricating perovskite layer.

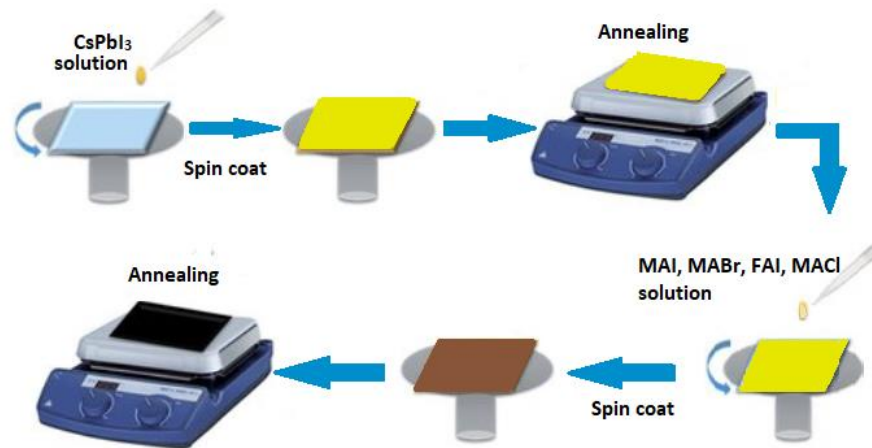


Figure 3.2: Two-step deposition method

Next, Spiro-OMeTAD solution ($50\mu\text{l}$) as a hole transport layer was spin-coated at 3000 rpm for 30 sec in a glove box. After depositing all layers, devices were oxidized by using oxygen gun and kept in an oxygen envelope for 12 hrs. After 12hrs of oxidation Silver layer as a metal electrode was deposited by thermal evaporation with the help of shadow mask. All solutions were filtered out before spin coating with a hydrophobic syringe filter having a pore size of $0.2\mu\text{m}$. Figure 3.3 a) Shows the device architecture of fabricated device which has planar n-i-p structure b) shows the perovskite layer thin film and c) shows the fabricated cells.

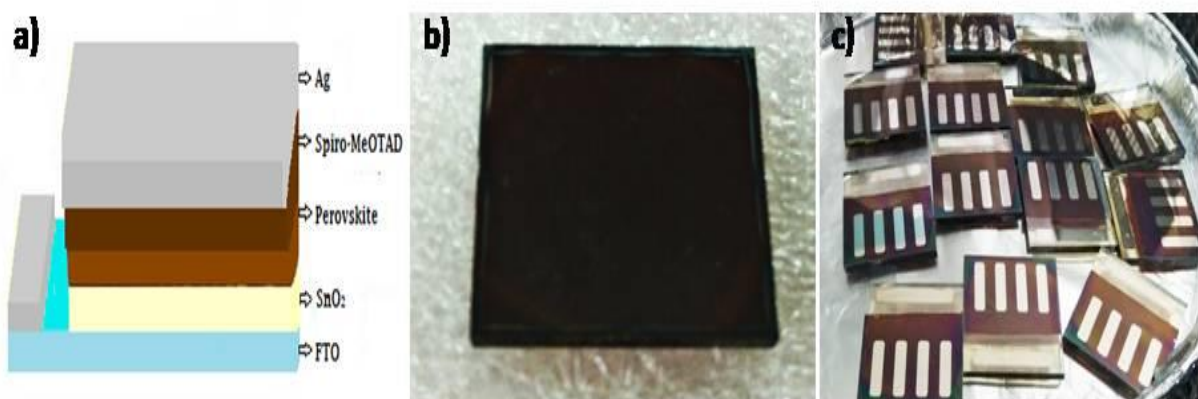


Figure3.3: a) Device architecture (n-i-p) b) Perovskite layer coated film c) Fabricated PSC device

3.2 Deposition techniques:

3.2.1 Spin coating:

It is the simplest technique employed to fabricate thin films on flat substrates. The solution is applied with the help of pipette on to the center of a substrate which involves the spinning of the substrate at a high rate and gives a uniform film. Centrifugal force is produced by the spinning of a substrate and causes the solution to be spread evenly from the middle. Spinning is continued till the appropriate thickness is obtained. Main factors such as spinning speed, viscosity of a fluid and surface tension determines the thickness of a film. Spin coating is generally used in micro-fabrication, where thin film thicknesses below 10nm can be achieved [76]. This technique is divided into the types of static and dynamic. Static spin coating is to coat a whole substrate with the solution before starting a spin coating. While a dynamic spin coating can be achieved at a low speed usually 500rpm.

Spin coating is advantageous due to less loss of materials during coating compare to the vapor-phase deposition. Despite its advantages spin coating have some drawbacks, the main drawback is the size of a substrate. For larger size, it is difficult to achieve thin film by using high-speed spinning. There can also be a possibility of the presence of contaminants [77]. Spin coater with vacuum pump is shown in figure 3.4.

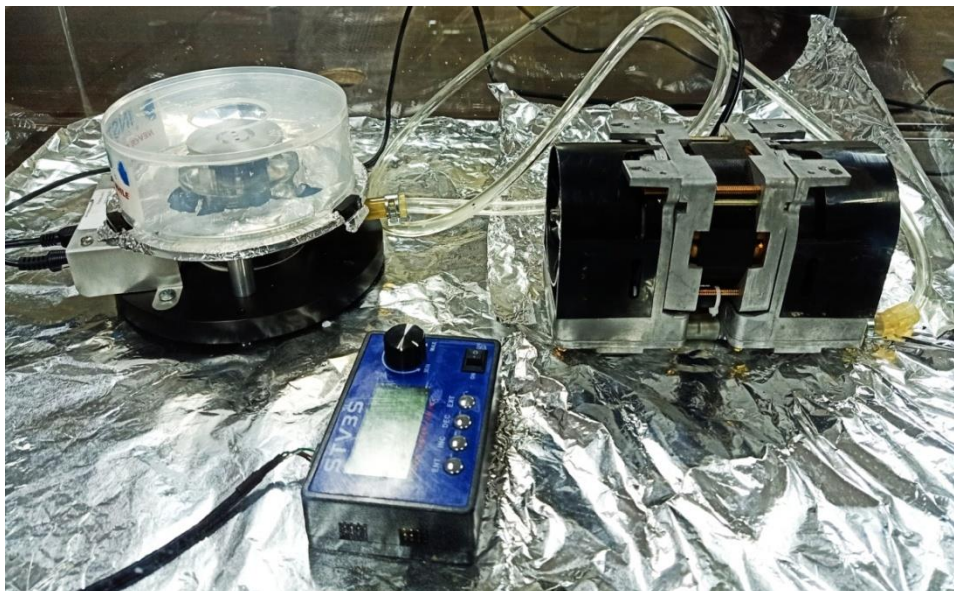


Figure 3.4: Spin coater

3.2.2 Thermal evaporation:

It is a simple approach of physical vapor deposition (PVD). It involves source materials for evaporation in a vacuum chamber containing pressure below 1×10^{-4} Pa and the evaporated atoms precipitated on a substrate [78]. Metals and non-metals both can be deposited by thermal evaporation. This technique is more useful to deposit metallic contact layer for thin-film devices i.e. solar cells, OLEDs, thin-film transistors. Basically, air is removed from the vacuum chamber using vacuum pumps. The metal source material in a little amount is placed in a vessel called boat and the boat is heating by flowing a large electric current across it, this process is called resistive heating. The boat is usually made up of tungsten because its melting point is very high as compared to the source materials and it is electrically conductive allowing resistive heating to occur. When a boat heats up it evaporates ultra-high purity source metal to gas, the gas atoms pass through the vacuum into a vacuum chamber and when these atoms strike to the substrate they precipitate and form a thin film on a surface of the substrate. Masks can be used to define the areas on substrates for desired purposes. This technique is the cheapest out of all physical vapor deposition techniques and can still give high purity thin vacuum coating. Thermal evaporator used for depositing the silver layer is presented figure 3.5.



Figure 3.5: Thermal evaporator

3.3 Characterization Techniques:

Characterization techniques are most important which is required to characterize the samples. It describes the surface morphology, structure, composition of elements, physical and magnetic properties. Brief descriptions of the techniques which are used to characterize the device are:

- i. XRD
- ii. SEM
- iii. UV-vis spectroscopy
- iv. J-V measurements

3.3.1 XRD:

A dominant advantageous method (X-ray diffraction) basically utilized to indicate crystallinity of materials and can provide details about the phases, unit cell dimensions,

structures and some other variables like crystal defects, average grain size and crystallinity. When a constructive interference appears XRD is predicted. In a sample, monochromatic X-ray beam from every set of lattice plane is dissipated at certain angles. For a given Bravais lattice, its lattice plane is a plane whose intersections are periodic with a lattice. Two adjoining planes having a distance which is interplanar spacing (d_{hkl}) with the Miller indices of suitable lattice planes [79]. In lattice planes, the peak intensities can be found from the atomic positions.

X-rays involve electromagnetic radiation of lower wavelength but have a similar nature as light. X-rays are generated when highly energized charged particles collide with the metal target.[80]

➤ **Measurement of crystals size:**

The average size of a crystal is evaluated by the Scherrer equation:

$$t = \frac{k\lambda}{\beta \cos\theta}$$

In this equation, t shows the crystal thickness, β is a peak width (FWHM), k is a Scherrer constant, λ is a X-ray wavelength and θ is a Bragg angle [81]. K is dependent on indexes of diffraction lines and shape of the crystal. From the recent reports, it is clear that k also depends on a crystallite size distribution of the powder [82]. Generally, K lies between 0.8 and 1.39; also, it is close to 1 for spherical particles. This formula describes about the size of particle. For the confined scattering of a particle size, influence of strain-induced is minimal.

➤ **Bragg's Law:**

It is stated as when an X-ray falls onto a surface of crystal, its incidence angle θ will reflect back with same of scattering angle θ . Constructive interference will take place when a (d) path difference is equivalent to the (n) whole number of a wavelength (λ). Figure 3.6 shows the two X-ray beams 1 and 2, which are reflected from adjoining planes A and B, defining the reflection angle is equivalent to the incidence angle. So the law can be written as:

$$2d\sin\theta = n\lambda$$

Where, $n=0, 1, 2\dots$ for $n=2$, d-spacing is halved, like $2\lambda = 2d\sin\theta$ is equivalent to $\lambda = 2\left(\frac{d}{2}\right)\sin\theta$

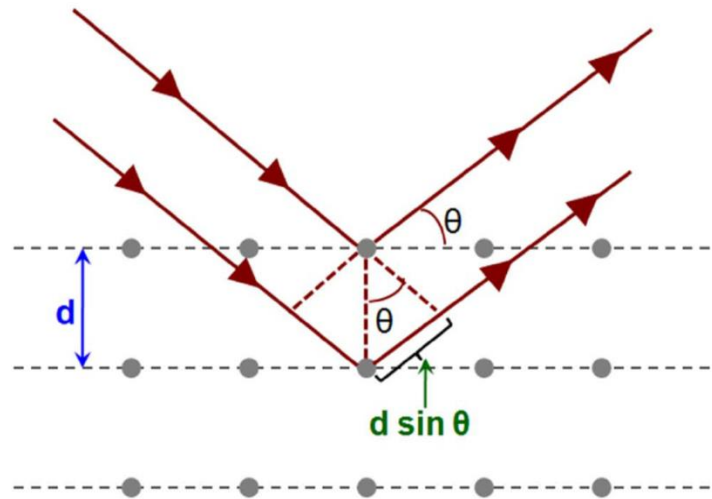


Figure 3.6: General schematic of Bragg's law [83]

For the measurement of a sample, sample was measured in thin-film configuration. Thin film was placed in a sample holder. Highly energized electrons fall on surface, bound electrons from the inner shell of atoms knocked off. X-rays are emitted, when electrons encounter a transition from higher shells into the lower shells. X-rays which was used are Cu $K\alpha$. Constructive interference produced when incident rays interact with the sample. By varying angle 2θ from 5° to 70° x-ray patterns were obtained. The incoming and outgoing angle of a beam is constantly fluctuating during a scan. To generate a focused beam, collimators are embodied in the beam direction. Figure 3.7 represents the X-ray diffractometer.



Figure 3.7: Bruker D8 Advance X-ray Diffractometer

3.3.2 SEM:

SEM (Scanning electron microscopy) provides a significant deal of information and exceeds most of the limitations of the optical microscopy. It gives data about topography, morphology, composition and crystallographic information of the material. The general layout of SEM which includes electron gun, anode, condenser and objective lens, scan coils, motorized stage, scan generator, amplifier and x-ray, secondary electron and backscattered electron detectors is shown in figure 3.8. It uses an intense ray of highly energized electrons induced by electron gun to generate an image of the sample. When electrons combine with the specimen, characteristic x-ray, backscattered and secondary electrons are generated [84]. A standard instrument accompanied by a metal plate with an off-center slot equipped in part

of the scintillator Faraday cage which collects secondary and scattered electrons. When an incident electron changes its path and loses some energy, secondary electrons are generated. These electrons are the most used imaging signals in SEM because each incident electron can generate several secondary electrons. When an incident electron collides with the atom in a sample, it loses some energy and scattered backwards which results in backscattered electrons. After the generation of a secondary electron, atom in the sample get de-energized which results in characteristic X-rays [85].

Scanning electron microscopy is a powerful analytical tool with a wide range of analytical, commercial and industrial applications. Modern SEMs produce data in digital formats which are highly portable. Figure 3.9 is representing a FE-SEM JEOL-JSM-6701F which is used for SEM analysis.

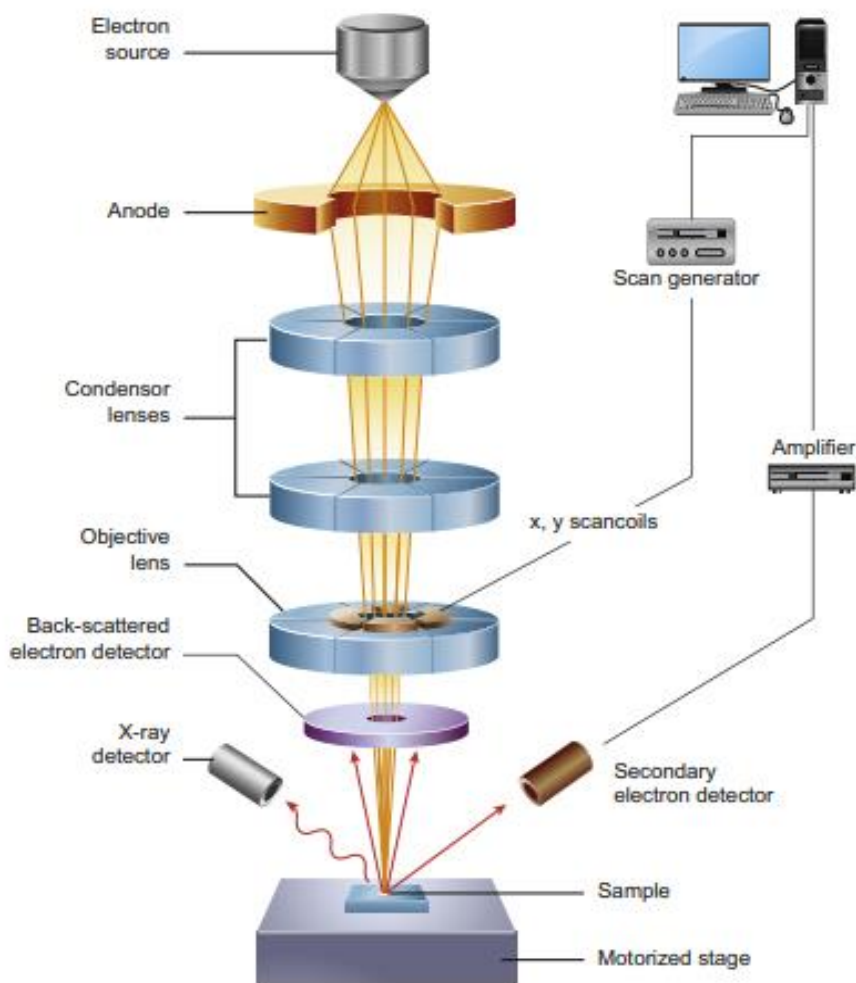


Figure 3.8: Diagrammatic representation of SEM [86]

➤ **EDS:**

It is used by SEM for the construction of elemental maps, which precisely symbolize elements distribution within the samples. The more frequent use of EDS (Energy-Dispersive X-ray Spectroscopy) is mineral orientation, morphology, contrasts and elemental analysis. EDX can be used for qualitative as well as quantitative analysis. EDX uses X-rays to distinguish the elements and the proportions of these elements in the specimen [87]. EDX analysis generates the data which contains spectra with peaks revealing all the distinct elements which occupy in the sample. Sample's elemental configuration is estimated through evaluating the characteristics x-ray energy and x-ray intensity of individual element. Energy dispersive spectrometer is used to estimate the quantity of x-rays energy radiated from a specimen [88].

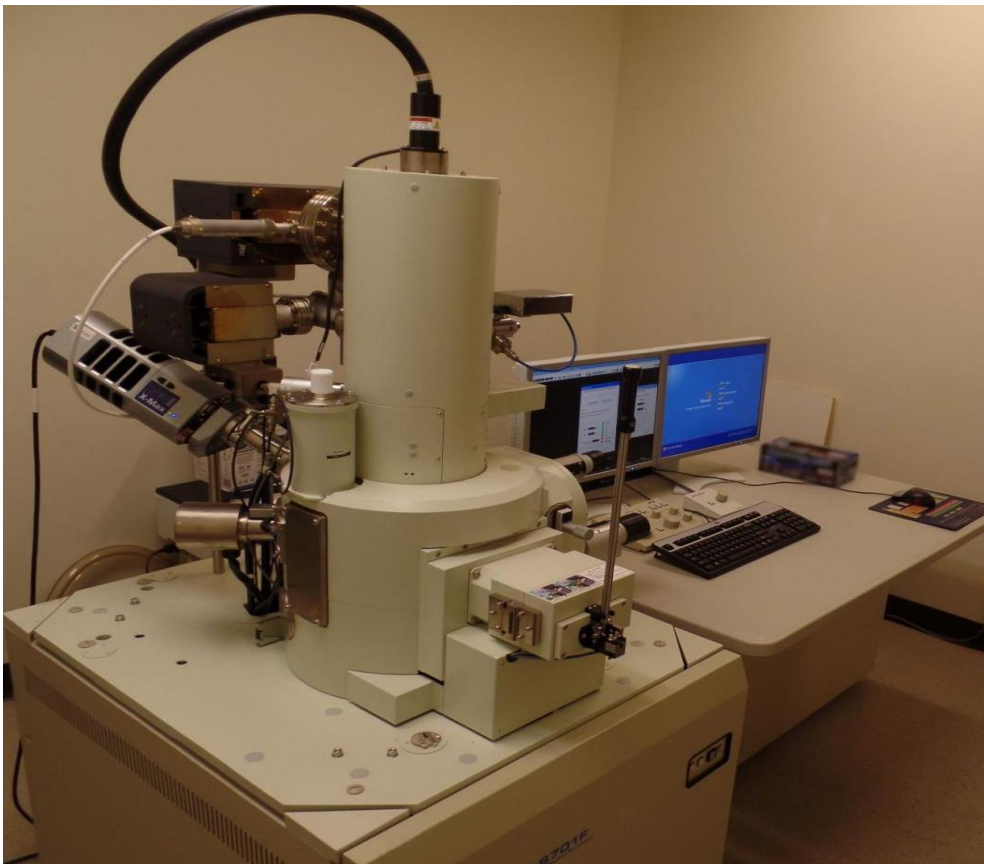


Figure 3.9: FE-SEM Apparatus

3.3.3 UV-VIS Spectroscopy:

Ultraviolet visible spectroscopy comprises the bulk of electronic and vibrational mode measurement techniques. Uv-vis spectroscopy utilizes the ultraviolet visible range of the light. The range of ultraviolet is 190-380nm and for visible it is between 380-750nm [89]. Ground to excited energy state transition is about an electronic energy level so electrons being promoted to excited energy state and then coming back again. In this technique amount of light absorbed or transmit as a function of wavelength can be measured. This is performed by measuring the light intensity which travels by a sample regarding a light intensity across a blank or reference sample. This method is useful for various sample types like glass, thin-films, liquids and solids. Figure 3.10 demonstrates the UV-Visible diode array spectrophotometer (Agilent 8453).



Figure 3.10: Uv-visible spectrophotometer (Agilent 8453)

➤ Working principle:

Figure 3.11 shows two lamps that are using for the incidence of light. D2 lamp emits ultraviolet light while Tungsten lamp generates visible light. When light falls on monochromator it passes through a prism that categorize a light into dissimilar wavelengths, then only a light of one specific wavelength allows to pass through a beam splitter and this beam splitter splits the beam into two different rays with same intensities [90] When this light of specific wavelength hits a molecule that molecule gets excited and jumps out from lower

to higher energy state and absorbs particular light energy. When light passes through the specimen, electron absorbs some quantity of the light and remaining light transmits, so the intensity of light is lost but when light passes through the reference, its intensity remains the same because there was no absorption occur. Then the detector detects all the data and gives measurements of absorbance vs wavelength.

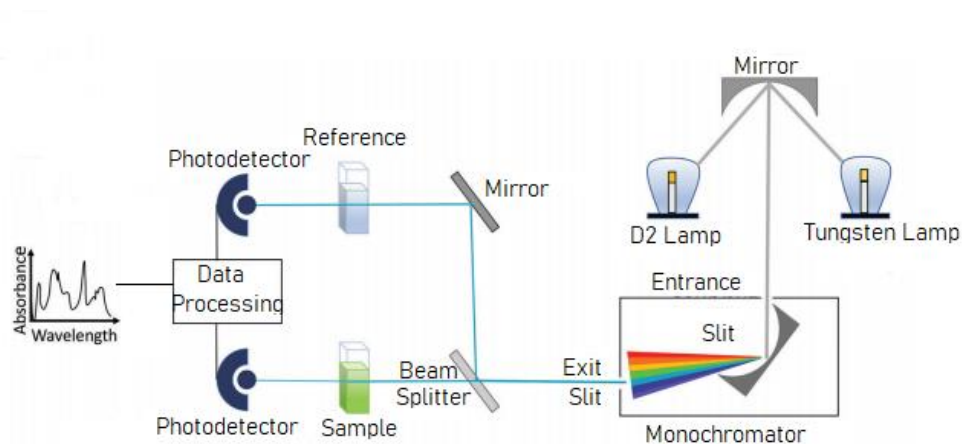


Figure 3.11: Working representation of UV-Visible spectroscopy

➤ **Beer Lambert’s Law:**

When a homogeneous light travel through an absorbing medium, the absorbance is equivalent to the path length of light which is similar to the cuvette width and also proportional to the concentration (c) of the sample used in the experiment. It can be written as,

$$A = \epsilon cl$$

Where ϵ is the proportionality constant which is called molar extinction coefficient [91] and absorbance A can be defined as,

$$A = \log_{10} \left(\frac{I_0}{I} \right)$$

Here, I_0 and I shows the incident intensity and transmitted intensity respectively. So, it can be written as,

$$A = \log_{10} \left(\frac{I_0}{I} \right) = \epsilon cl$$

➤ **Tauc Plot Method:**

Tauc plot method is an appropriate and elementary method to probe the visible bandgap of a thin-film material. A fundamental approach for a Tauc investigation is to obtain absorbance information for specimens which traverse the energies ranges from low to high bandgap transition. The strength of absorption depends on the distinction among the bandgap and photon energy which is;

$$(\alpha hv)^{\frac{1}{n}} = A (hv - E_g)$$

In the above equation,

hv = incident photon energy

n = photon's frequency

α = coefficient of absorption

A = proportionality constant

E_g = optical bandgap (calculated from a slope)

Exponent's value shows the identity of the electronic transition, it can be direct, indirect, allowed and forbidden. Photon's frequency is $n=3$, $n=3/2$, $n=2$ and $n=1/2$ for indirect forbidden, direct forbidden, indirect allowed and direct allowed transitions respectively [92].

3.3.4 Current voltage characteristics:

It is a fundamental technique to test the PCE of a solar cell in which voltage is employed across the solar cell device and current can be measured via it. Computer shows all the data of measurements. Setup of CH1660D workstation is shown in figure 3.12. The device used for the measurement of I-V curve is a source measurement unit with a solar stimulator having a solar spectrum of AM1.5G of power 100 mWcm^{-2} .

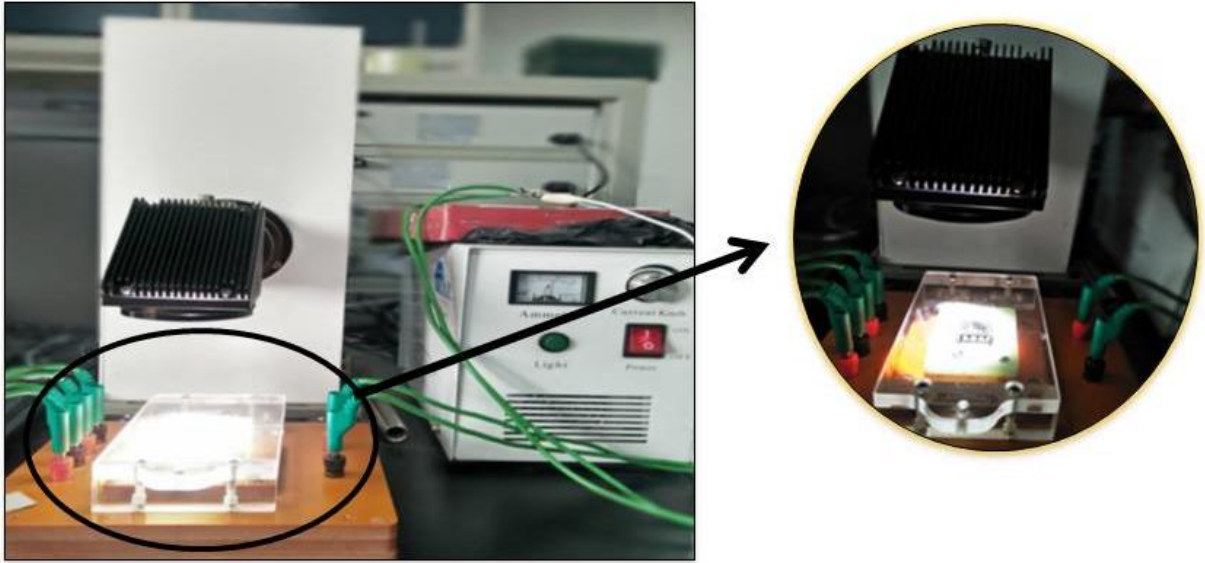


Figure 3.12: CH1660D electrochemical workstation with solar simulator

By using these measurement techniques some major variables of a solar cell are determined such as (V_{oc}) Open-circuit voltage, (J_{sc}) Short-circuit current density, (FF) Fill factor and Power conversion efficiency (PCE) [93]. Generally, a current is converted to a current density (J) by considering a cell active area, which leads to a J - V curve. Power is maximum at a bend tip of the I- V curve (figure 3.13) which is called a maximum power point and represented by P_m .

$$P_m = I_m \times V_m$$

V_{oc} is the voltage if there is no external current. I_{sc} is the current when there is no external voltage. It depends on the temperature of a cell and its technology. J_{sc} is current generated when no voltage is employed, and it is a ratio of I_{sc} to the surface area of a device.

$$J_{sc} = \frac{I_{sc}}{A}$$

Fill factor identifies the nature of a solar cell. It also describes the squareness of a I- V curve. It is obtained by differentiating a maximum power to the product of V_{oc} times J_{sc} .

$$FF = \frac{P_m}{J_{sc} \times V_{oc}}$$

The PCE denoted by η is a proportion between the maximum powers to input power.

$$\eta = \frac{P_m}{P_{in}} = \frac{V_{oc} \cdot J_{sc} \cdot FF}{P_{in}}$$

These parameters J_{sc} , V_{oc} and FF , can be used to examine a quality of the solar cell. For example, the J_{sc} of the device is strongly dependent on the absorptance and the E_g of the photo absorber, the FF can indicate whether the solar cell has charge-carrier collection, or transfer, problems and recombination effects can be observed by the appearance of a J-V curve as well as by a lowered V_{oc} [45].

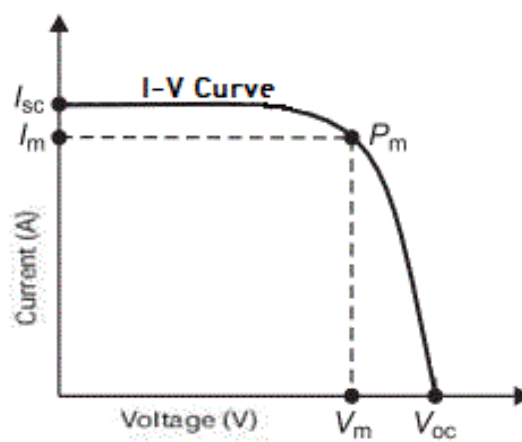


Figure 3.13: Representation of I-V curve

Chapter 4

Results and Discussion:

Discrete characterization techniques were conducted to study the morphology, composition, structural properties and the main technique which is used to test the conversion efficiency of PSC is presented in this chapter. Further stability curves were determined from J-V curves.

4.1 Sample detail:

Description of samples is given below.

Table 3: Sample detail

Sr. No.	Device	Concentration
1	A	MACl ₀
2	B	MACl _{0.02}
3	C	MACl _{0.05}
4	D	MACl _{0.07}

4.2 X-Ray Diffraction (XRD):

Investigation of the structural properties of composed perovskite layers was implemented by using XRD (BRUKER D8-ADVANCE). The sources Cu K α as an X-rays were used to conduct XRD. The wavelength of these X-rays is 1.54Å. Figure 4.1 corresponds to the XRD of perovskite layers. The main diffraction peak of PbI₂ at the angle of 12.7° corresponds to (001) plane is shown in the figure. The other PbI₂ peak of (002), (003) and (004) at the angle of 24.3, 38.4 and 52.4° is shown. PbI₂ peaks correspond to JCPDS07-0235 card [94]. These peaks of PbI₂ reveal that it is not fully converted into the perovskite. Moderate PbI₂ residuals are beneficial for the device performance as reported but high content of PbI₂ residual can reduce the performance of the device as reported [95]. Perovskite peaks represented by (110), (220), (310), (312) and (224) planes at the angle of 14.02°, 28.1°, 31.6°, 35.3° and 40.3° respectively appear in the XRD. These diffraction peaks confirm the formation of perovskite. Highly intense peaks of perovskite are shown by device B and D which exhibits high

crystallinity. Other small peaks assigned to the ITO substrate. Device A and D reveals the highly intense peaks of PbI_2 . It depends on the concentration of MACl. Little quantity of MACl is helpful for the transformation of PbI_2 into perovskite which also affects the intensity. By using a high concentration of MACl, PbI_2 increases as shown in device D.

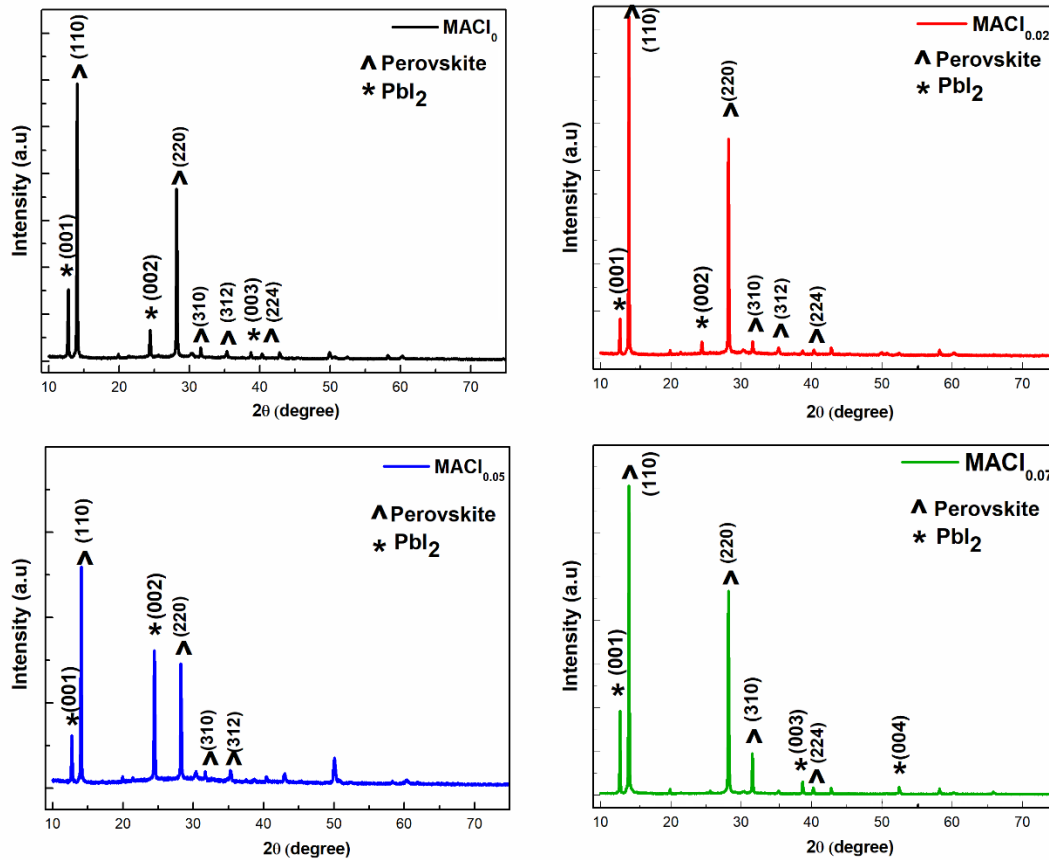


Figure 4.1: XRD pattern of the perovskite layer of four samples

4.3 Scanning Electron Microscopy (SEM):

The measurements of SEM were implemented by using FE-SEM (JEOL-JSM-6701F) with an accelerating voltage of 10kV. Figure 4.2 shows the SEM images of perovskite layers having four concentrations of MACl with the magnitude of X20,000. Figure 4.2 A, B, C and D shows the concentrations of MACl_0 , $\text{MACl}_{0.02}$, $\text{MACl}_{0.05}$, and $\text{MACl}_{0.07}$ respectively. There are pinholes (figure A, D) which act as a recombination centre of electrons and holes, while figure B, C has no pinholes. Also, device B shows the larger grain size as compared to the device C. Larger grain size means fewer grain boundaries which can reduce the recombination process because it is easy for electrons to pass through fewer boundaries. Increase in grain boundaries can cause strong non-radiative recombination of electrons and

holes. Device A also reveals a larger grain size but because of the presence of pinholes, electrons and holes can recombine at the ETM layer and it causes degradation of a device. There are also content of PbI_2 residual (white phase) in all devices but more prominent at device B and C which depends on the MACl concentration. Formation of PbI_2 is around the grain boundary of perovskites in device A and D but in device B and C, it is present on the grains. These PbI_2 phases are due to the decomposition of perovskite by annealing [65]. A small quantity of PbI_2 residual is helpful for the passivation of a grain boundary but high content of PbI_2 residual may affect the device performance. For the deposition of perovskite material, a two-step technique was used due to which MACl precursors will contact PbI_2 surface which creates perovskite at the surface.

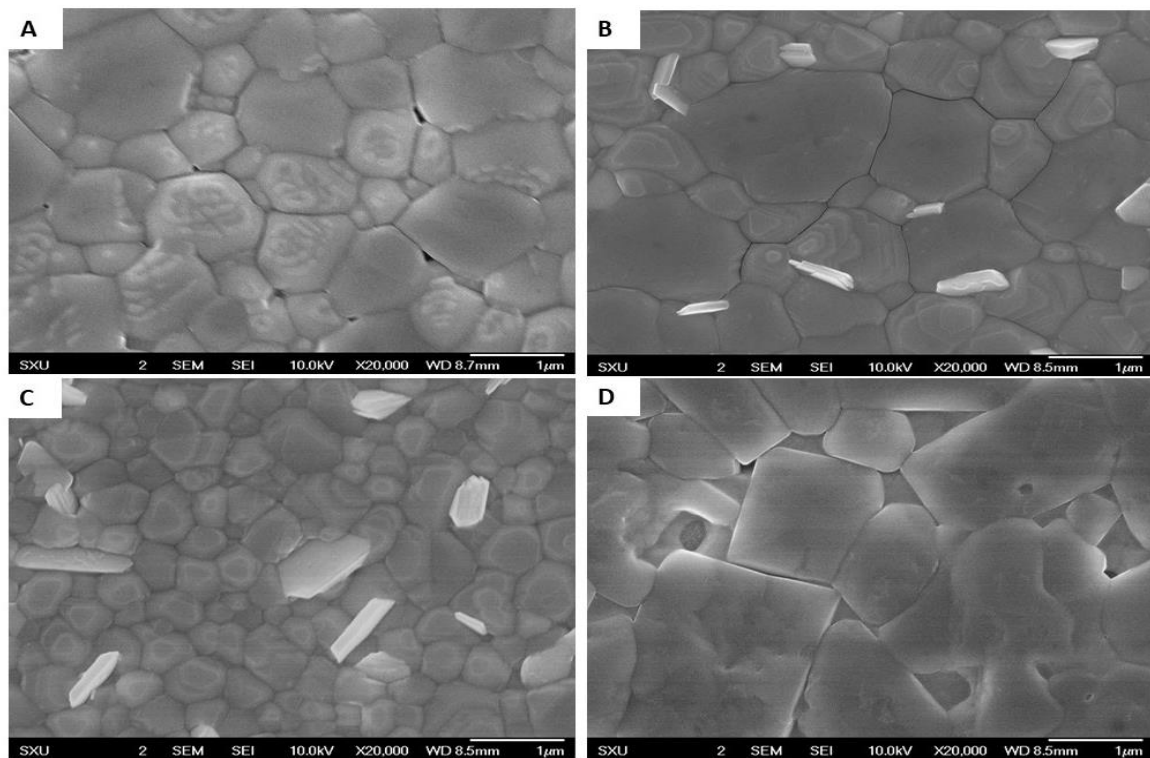


Figure 4.2: SEM images of four perovskite layer samples with a magnitude of X20,000

4.4 UV-VIS Spectroscopy:

A UV-Visible spectrum is an important technique to examine the perovskite layer's absorption. The absorption spectra were determined by Agilent 8453 Uv-visible diode array spectrophotometer. Bandgaps of perovskite are also determined from UV-Vis spectra.

4.4.1 UV-VIS of Perovskite layer:

UV-Vis spectra of four devices are represented in figure 4.3. By changing the concentrations of MAI there is not much influence of absorption. The plateaus and quick arising parts in the domain of 450nm-780nm of mixed halide perovskites are shown which suggests the good light absorption and it is larger than the other perovskites like MAPbI₃ [96]. Two main peaks of devices A, B, C, D are 478nm and 764, 768, 762, 767nm clearly visible in the spectra.

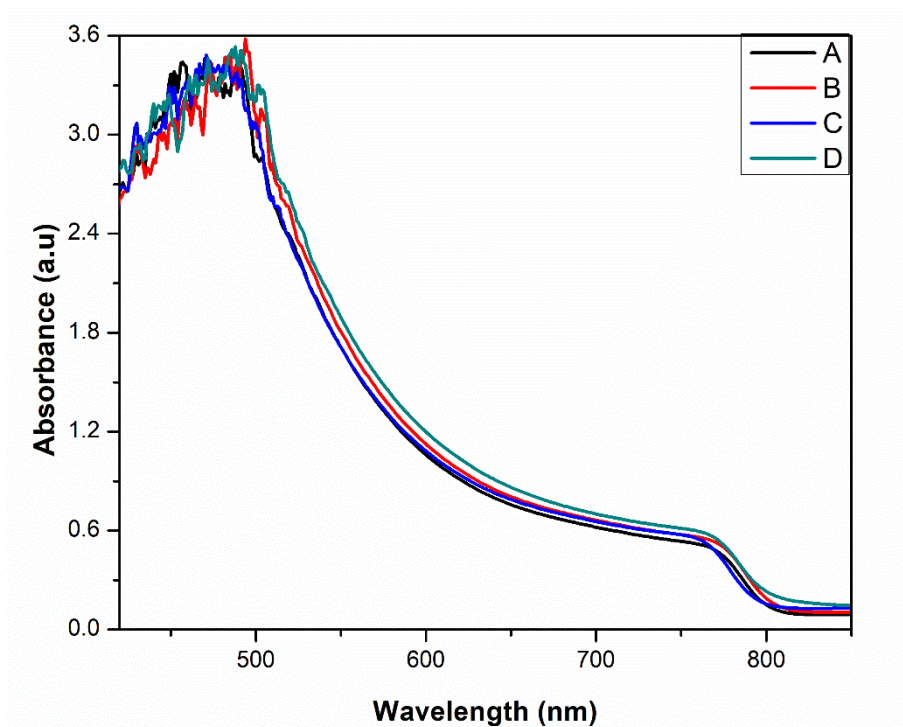


Figure 4.3: Uv-visible spectra of four perovskite layers

4.4.2 Bandgap of Perovskite Material:

Perovskite materials can tune the bandgaps ranges from 1.15-3.06eV. It occurs by switching the cations, halides or metals of ABX₃ [97]. By using the Tauc Plot, direct bandgaps of perovskite devices are calculated in figure 4.4. Indirect bandgaps are also calculated which is about 1.53eV. As mentioned in UV-Vis spectra of perovskites there is no obvious change in the absorption with the different concentrations of MAI so due to this reason, bandgaps of perovskite materials are almost the same. Direct bandgap of four devices such that A, B, C and D are 1.56, 1.55, 1.57 and 1.55eV respectively. It is nearer to the bandgap given by S-Q theory. This bandgap is similar to the other perovskite's bandgap like 1.5-1.6eV of MAPbI₃. Starting with the deposition of CsPbI₃ on a substrate which exhibits the bandgap of 1.73eV, further mixed precursor solution was deposited and formed a perovskite which reduces the overall bandgap to 1.55eV.

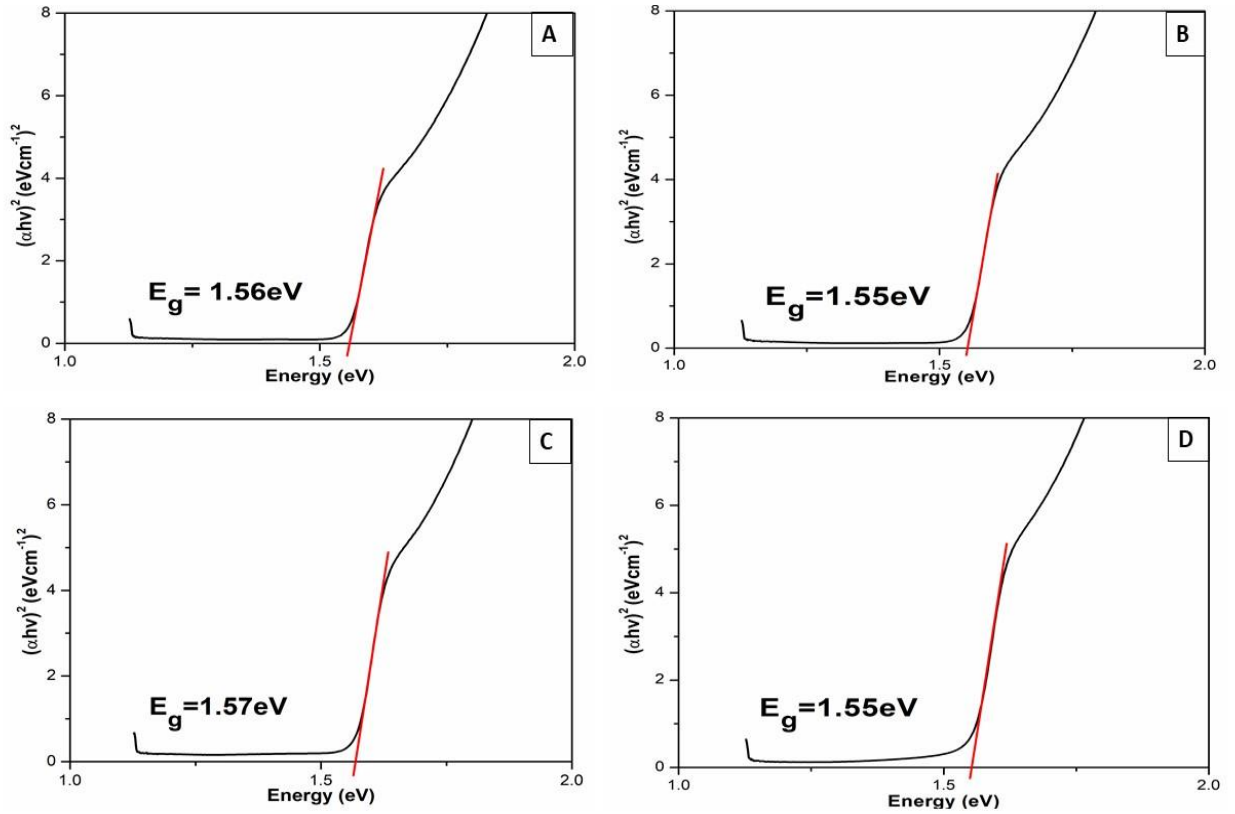


Figure 4.4: Calculated Bandgaps of four perovskite samples

4.5 J-V measurements:

To check the efficiency of a solar cell, J-V measurements are the crucial part in the characterization of devices. The (J-V) photocurrent density-voltage measurements of the PSC were implemented by using electrochemical workstation CHI660D (computer-controlled) in the ambient atmosphere. The intensity of incident light was set under AM 1.5G (100mWcm^{-2}). The scan rate was measured as 0.05 V/s . An active area of 0.09cm^2 was controlled by applying the black mask.

4.5.1 J-V curves:

Current density-voltage characteristics of device A, B, C and D are appeared in figure 4.5. FF is an important parameter which defines the quality of a device. Device B and C have a high FF and V_{oc} as compared to device A and D. The PCE of fabricated solar cells are 14.33, 16.42, 16.06 and 13.9% respectively. Photovoltaic parameters used to determine PCE are summarized in Table 4. According to these parameters, PCE of sample B is better than the other devices.

Table 4: Summarized photovoltaic parameters with PCE

PSC	V _{oc} (V)	J _{sc} (mAcm ⁻²)	FF	PCE (%)
A	0.98	24.1	0.607	14.33
B	1.002	23.9	0.686	16.42
C	1.009	22.3	0.713	16.04
D	0.971	23.6	0.606	13.88

PCE of a solar cell can be determined by using the equation:

$$\eta = \frac{V_{oc} \cdot J_{sc} \cdot FF}{P_{in}}$$

The standard AM1.5 spectrum has P_{in} of 100mW/cm².

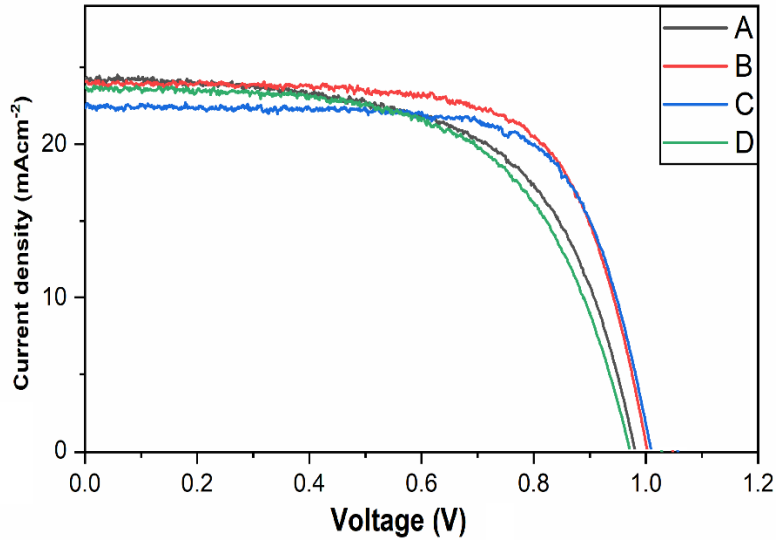


Figure 4.5: J-V measurements of PSCs

4.5.2 Stability Curves:

For device stability test, PCS's were placed unencapsulated under the dark environment in a moisture-resistant box with a controlled temperature of 25°C and relative humidity of 20%. Figure 4.6 reveals the stability curves of fabricated devices. PCE was measured for six days continuously in the air. Device A shows quick degradation while device B exhibits better stability compared to the other devices. Also, device B shows saturation after the six days,

which prevents the further degradation of PSC. Device A exhibits the PCE decay from 14 to 5%, B reveals the decay from 16 to 11%, C shows the decay from 16 to 9% and device D indicates the PCE decay from 13 to 8%.

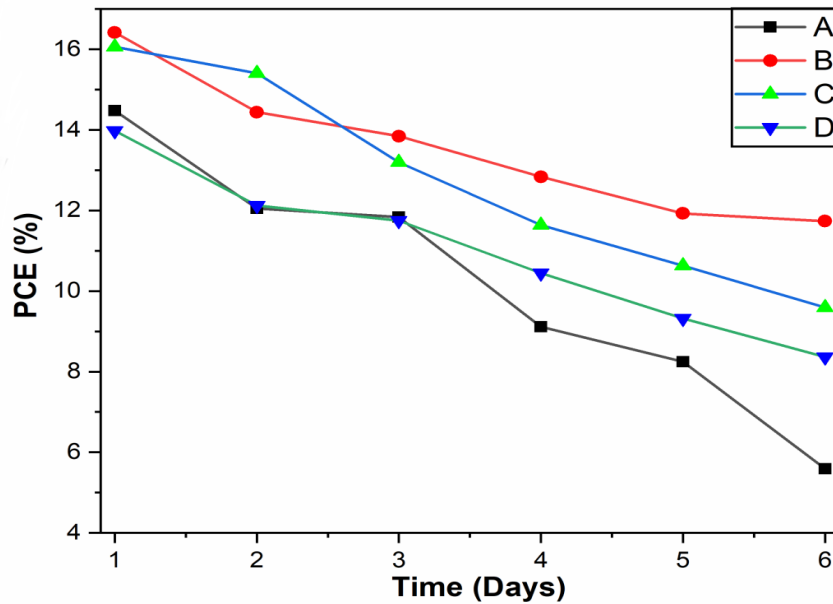


Figure 4.6: Stability curves of PSC

PSC (without encapsulation) with the normalized values attained from the J-V curves are demonstrated in figure 4.7. PCE of devices A, B, C and D was 38%, 71%, 60% and 59% of the original PCE. Device A shows high instability and device B exhibits better stability as compared to the other devices.

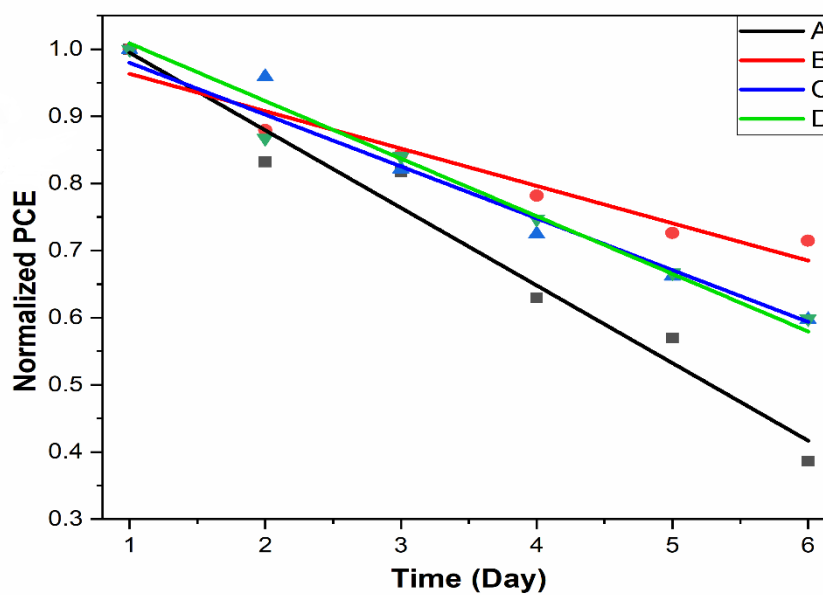


Figure 4.7: PSC with normalized PCEs

Chapter 5

Conclusion:

Conventional (n-i-p) architecture FTO/SnO₂/Perovskite/Spiro-MeOTAD/Ag was fabricated. Mixed cations and halide perovskites appeared with better stability as compared to the single anion/halide perovskite. In this work, mixed cation and halide perovskites were prepared by utilizing a two-step deposition technique with different concentrations of MAI. In the two-step method, first CsPbI₃ shows the δ -yellow phase which later converts to the α -black phase by deposition and annealing of another precursor solution. The molar ratio of MAI was taken as 0, 0.025, 0.05 and 0.07M/L.

XRD confirms the perovskite layer formation which also contains PbI₂ residuals. Highly intense diffraction peaks of PbI₂ have shown in device A and D which can cause degradation of the device. Diffraction peaks of perovskite with high intensity appear in device B and D.

Morphological examination of the perovskite layer was confirmed by SEM which reveals the presence of pinholes in device A and D while device B and C have no pinholes. The existence of PbI₂ residuals is also confirmed in all devices which indicate the partial conversion of PbI₂ into perovskite. Device B shows a larger grain size as compared to the device C. Larger grain size corresponds to the fewer grain boundaries which reduce the recombination process for electrons and holes.

The UV-visible spectrum indicates the absorption of a perovskite layer in the visible region of 450nm-780nm. Different concentrations of MAI barely affect the absorption. Two main peaks of four devices exist at 478nm and 764, 768, 762, 767nm respectively. The bandgap of four devices was determined by using Tauc plot which comes out to be 1.56, 1.55, 1.57 and 1.55eV respectively. This bandgap is near to the bandgap given by S-Q theory.

PCE was identified by J-V measurements which exhibits the highest efficiency 16.42% correspond to device B. Another devices A, C and D exhibit the PCE of 14.33, 16.02 and 13.88% respectively. But device C shows a better fill factor than device B.

Stability curves were obtained from J-V measurement without encapsulated placed in a dark moisture-resistant box with the RH of 20%. Device A, B, C and D exhibits the PCE decay from 14 to 5%, 16 to 11%, 16 to 9% and 13 to 8% respectively.

Normalized values of PSCs were also determined by J-V curves which conclude the PCE of devices A, B, C and D was 38%, 71%, 60% and 59% of the original PCE.

The above-concluded results indicate that PCE of devices was increased and decreased without the influence of bandgap. Grain functionalization was carried out by changing the concentration of MACl because MACl helps in the enhancement of crystal nucleation process. Overall device B shows better efficiency and stability than the other devices. So the concentration of MACl may vary between 0.025-0.05M/L for the best efficiency which may attempt in the future. For further enhancement in the efficiency of PSC, surface functionalization would be beneficial.

5.1 References:

1. Abou-Ras, D., T. Kirchartz, and U. Rau, *Advanced characterization techniques for thin film solar cells*. 2016: John Wiley & Sons.
2. Yoshikawa, K., et al., *Silicon heterojunction solar cell with interdigitated back contacts for a photoconversion efficiency over 26%*. *Nature energy*, 2017. **2**(5): p. 17032.
3. Editorial, *Decade of Perovskite Photovoltaics*. *Nat. Energy*, 2019. **4**: p. 1.
4. Li, X., et al., *A vacuum flash-assisted solution process for high-efficiency large-area perovskite solar cells*. *Science*, 2016. **353**(6294): p. 58-62.
5. King, R.R., et al. *Band-gap-engineered architectures for high-efficiency multijunction concentrator solar cells*. in *24th European Photovoltaic Solar Energy Conference and Exhibition, Hamburg, Germany*. 2009.
6. Sha, W.E., et al., *The efficiency limit of CH₃NH₃PbI₃ perovskite solar cells*. *Applied Physics Letters*, 2015. **106**(22): p. 221104.
7. NREL, N., *Best Research-Cell Efficiency Chart*. 2019, US Department of Energy.
8. Hanusch, F., *Solution processed perovskite solar cells*. 2015, lmu.
9. Li, Z., et al., *Stabilizing perovskite structures by tuning tolerance factor: formation of formamidinium and cesium lead iodide solid-state alloys*. *Chemistry of Materials*, 2016. **28**(1): p. 284-292.
10. Koh, T.M., et al., *Formamidinium-containing metal-halide: an alternative material for near-IR absorption perovskite solar cells*. *The Journal of Physical Chemistry C*, 2014. **118**(30): p. 16458-16462.
11. Yin, W.-J., et al., *Halide perovskite materials for solar cells: a theoretical review*. *Journal of Materials Chemistry A*, 2015. **3**(17): p. 8926-8942.
12. Liu, H., et al., *Nano-structured electron transporting materials for perovskite solar cells*. *Nanoscale*, 2016. **8**(12): p. 6209-6221.
13. Habisreutinger, S.N., et al., *Carbon nanotube/polymer composites as a highly stable hole collection layer in perovskite solar cells*. *Nano letters*, 2014. **14**(10): p. 5561-5568.
14. Kojima, A., et al., *Organometal halide perovskites as visible-light sensitizers for photovoltaic cells*. *Journal of the American Chemical Society*, 2009. **131**(17): p. 6050-6051.
15. Im, J.-H., et al., *6.5% efficient perovskite quantum-dot-sensitized solar cell*. *Nanoscale*, 2011. **3**(10): p. 4088-4093.
16. Chen, L.-C. and Z.-L. Tseng, *ZnO-based electron transporting layer for perovskite solar cells*. *Nanostructured Solar Cells*, 2017: p. 203.

17. Lee, M.M., et al., *Efficient hybrid solar cells based on meso-superstructured organometal halide perovskites*. *Science*, 2012. **338**(6107): p. 643-647.
18. Kim, H.-S., et al., *Lead iodide perovskite sensitized all-solid-state submicron thin film mesoscopic solar cell with efficiency exceeding 9%*. *Scientific reports*, 2012. **2**: p. 591.
19. Mali, S.S., et al., *In situ processed gold nanoparticle-embedded TiO₂ nanofibers enabling plasmonic perovskite solar cells to exceed 14% conversion efficiency*. *Nanoscale*, 2016. **8**(5): p. 2664-2677.
20. Zhu, L., et al., *Mesoporous BaSnO₃ layer based perovskite solar cells*. *Chemical Communications*, 2016. **52**(5): p. 970-973.
21. Shi, Y., et al., *CH₃NH₃PbI₃ and CH₃NH₃PbI_{3-x}Cl_x in Planar or Mesoporous Perovskite Solar Cells: Comprehensive Insight into the Dependence of Performance on Architecture*. *The Journal of Physical Chemistry C*, 2015. **119**(28): p. 15868-15873.
22. Shi, Z. and A.H. Jayatissa, *Perovskites-based solar cells: A review of recent progress, materials and processing methods*. *Materials*, 2018. **11**(5): p. 729.
23. Saliba, M., et al., *Incorporation of rubidium cations into perovskite solar cells improves photovoltaic performance*. *Science*, 2016. **354**(6309): p. 206-209.
24. Zhou, D., et al., *Perovskite-based solar cells: materials, methods, and future perspectives*. *Journal of Nanomaterials*, 2018. **2018**.
25. Anaraki, E.H., et al., *Highly efficient and stable planar perovskite solar cells by solution-processed tin oxide*. *Energy & Environmental Science*, 2016. **9**(10): p. 3128-3134.
26. Manspecker, C., *Role of the cation in hybrid organic-inorganic perovskite solar materials*. 2018.
27. Manspecker, C., et al., *Reliable annealing of CH₃NH₃PbI₃ films deposited on ZnO*. *The Journal of Physical Chemistry C*, 2016. **120**(12): p. 6377-6382.
28. Manspecker, C., et al., *Role of interface in stability of perovskite solar cells*. *Current Opinion in Chemical Engineering*, 2017. **15**: p. 1-7.
29. Meng, L., et al., *Recent advances in the inverted planar structure of perovskite solar cells*. *Accounts of chemical research*, 2016. **49**(1): p. 155-165.
30. Wu, C.-G., et al., *High efficiency stable inverted perovskite solar cells without current hysteresis*. *Energy & Environmental Science*, 2015. **8**(9): p. 2725-2733.
31. Kitazawa, N., Y. Watanabe, and Y. Nakamura, *Optical properties of CH₃NH₃PbX₃ (X= halogen) and their mixed-halide crystals*. *Journal of materials science*, 2002. **37**(17): p. 3585-3587.

32. Kulkarni, S.A., et al., *Band-gap tuning of lead halide perovskites using a sequential deposition process*. Journal of Materials Chemistry A, 2014. **2**(24): p. 9221-9225.
33. Stranks, S.D., et al., *Electron-hole diffusion lengths exceeding 1 micrometer in an organometal trihalide perovskite absorber*. Science, 2013. **342**(6156): p. 341-344.
34. Perovskite-Silicon, F.-T., *Development of High Efficiency Four-Terminal Perovskite-Silicon Tandems*. Ann Arbor, 2017. **1001**: p. 48106-41346.
35. Dualeh, A., et al., *Effect of annealing temperature on film morphology of organic-inorganic hybrid perovskite solid-state solar cells*. Advanced Functional Materials, 2014. **24**(21): p. 3250-3258.
36. Kim, H.-S., S.H. Im, and N.-G. Park, *Organolead halide perovskite: new horizons in solar cell research*. The Journal of Physical Chemistry C, 2014. **118**(11): p. 5615-5625.
37. Shin, S.S., et al., *Colloidally prepared La-doped BaSnO₃ electrodes for efficient, photostable perovskite solar cells*. Science, 2017. **356**(6334): p. 167-171.
38. Li, W., et al., *Enhanced UV-light stability of planar heterojunction perovskite solar cells with caesium bromide interface modification*. Energy & Environmental Science, 2016. **9**(2): p. 490-498.
39. Ito, S., et al., *Effects of surface blocking layer of Sb₂S₃ on nanocrystalline TiO₂ for CH₃NH₃PbI₃ perovskite solar cells*. The Journal of Physical Chemistry C, 2014. **118**(30): p. 16995-17000.
40. Niu, G., X. Guo, and L. Wang, *Review of recent progress in chemical stability of perovskite solar cells*. Journal of Materials Chemistry A, 2015. **3**(17): p. 8970-8980.
41. Grancini, G., et al., *One-Year stable perovskite solar cells by 2D/3D interface engineering*. Nature communications, 2017. **8**(1): p. 1-8.
42. Shao, S., et al., *Highly reproducible Sn-based hybrid perovskite solar cells with 9% efficiency*. Advanced Energy Materials, 2018. **8**(4): p. 1702019.
43. Snaith, H.J., et al., *Anomalous hysteresis in perovskite solar cells*. The journal of physical chemistry letters, 2014. **5**(9): p. 1511-1515.
44. Herz, L.M., *Charge-carrier mobilities in metal halide perovskites: fundamental mechanisms and limits*. ACS Energy Letters, 2017. **2**(7): p. 1539-1548.
45. Sveinbjörnsson, K., *Preparation and Characterization of Lead Halide Perovskites: Towards sustainable, cost-effective and upscalable solar cell manufacture*. 2018, Acta Universitatis Upsaliensis.

46. Raveau, B., *The perovskite history: More than 60 years of research from the discovery of ferroelectricity to colossal magnetoresistance via high TC superconductivity*. Progress in Solid State Chemistry, 2007. **2**(35): p. 171-173.
47. Etgar, L., et al., *Mesoscopic CH₃NH₃PbI₃/TiO₂ heterojunction solar cells*. Journal of the American Chemical Society, 2012. **134**(42): p. 17396-17399.
48. Kim, H.-S., et al., *High efficiency solid-state sensitized solar cell-based on submicrometer rutile TiO₂ nanorod and CH₃NH₃PbI₃ perovskite sensitizer*. Nano letters, 2013. **13**(6): p. 2412-2417.
49. Ghanavi, S., *Organic-inorganic hybrid perovskites as light absorbing/hole conducting material in solar cells*. 2013.
50. Ku, Z., et al., *Full printable processed mesoscopic CH₃NH₃PbI₃/TiO₂ heterojunction solar cells with carbon counter electrode*. Scientific reports, 2013. **3**: p. 3132.
51. Aharon, S., B.E. Cohen, and L. Etgar, *Hybrid lead halide iodide and lead halide bromide in efficient hole conductor free perovskite solar cell*. The Journal of Physical Chemistry C, 2014. **118**(30): p. 17160-17165.
52. Eperon, G.E., et al., *Formamidinium lead trihalide: a broadly tunable perovskite for efficient planar heterojunction solar cells*. Energy & Environmental Science, 2014. **7**(3): p. 982-988.
53. Wang, K.-C., et al., *P-type mesoscopic nickel oxide/organometallic perovskite heterojunction solar cells*. Scientific reports, 2014. **4**: p. 4756.
54. Christians, J.A., R.C. Fung, and P.V. Kamat, *An inorganic hole conductor for organo-lead halide perovskite solar cells. Improved hole conductivity with copper iodide*. Journal of the American Chemical Society, 2014. **136**(2): p. 758-764.
55. You, J., et al., *Moisture assisted perovskite film growth for high performance solar cells*. Applied Physics Letters, 2014. **105**(18): p. 183902.
56. Bryant, D., et al., *A transparent conductive adhesive laminate electrode for high-efficiency organic-inorganic lead halide perovskite solar cells*. Advanced Materials, 2014. **26**(44): p. 7499-7504.
57. Wang, H.-H., et al., *Improving the TiO₂ electron transport layer in perovskite solar cells using acetylacetonate-based additives*. Journal of Materials Chemistry A, 2015. **3**(17): p. 9108-9115.
58. Zhang, J., et al., *Fast and low temperature growth of electron transport layers for efficient perovskite solar cells*. Journal of Materials Chemistry A, 2015. **3**(9): p. 4909-4915.
59. Roose, B., et al., *Enhanced Efficiency and Stability of Perovskite Solar Cells Through Nd-Doping of Mesostructured TiO₂*. Advanced Energy Materials, 2016. **6**(2): p. 1501868.

60. Yan, W., et al., *Increasing open circuit voltage by adjusting work function of hole-transporting materials in perovskite solar cells*. Nano Research, 2016. **9**(6): p. 1600-1608.
61. Wu, Y., et al., *Perovskite solar cells with 18.21% efficiency and area over 1 cm² fabricated by heterojunction engineering*. Nature Energy, 2016. **1**(11): p. 1-7.
62. Li, Y., et al., *50% Sn-Based Planar Perovskite Solar Cell with Power Conversion Efficiency up to 13.6%*. Advanced Energy Materials, 2016. **6**(24): p. 1601353.
63. Yin, X., et al., *One-step facile synthesis of a simple carbazole-cored hole transport material for high-performance perovskite solar cells*. Nano Energy, 2017. **40**: p. 163-169.
64. Lee, J., et al., *Achieving large-area planar perovskite solar cells by introducing an interfacial compatibilizer*. Advanced Materials, 2017. **29**(22): p. 1606363.
65. Jiang, Q., et al., *Planar-structure perovskite solar cells with efficiency beyond 21%*. Advanced materials, 2017. **29**(46): p. 1703852.
66. Liu, C., et al., *All-inorganic CsPbI₂Br perovskite solar cells with high efficiency exceeding 13%*. Journal of the American chemical society, 2018. **140**(11): p. 3825-3828.
67. Son, D.-Y., et al., *Universal approach toward hysteresis-free perovskite solar cell via defect engineering*. Journal of the American Chemical Society, 2018. **140**(4): p. 1358-1364.
68. Turren-Cruz, S.-H., A. Hagfeldt, and M. Saliba, *Methylammonium-free, high-performance, and stable perovskite solar cells on a planar architecture*. Science, 2018. **362**(6413): p. 449-453.
69. Chen, Z., et al., *Single-crystal MAPbI₃ perovskite solar cells exceeding 21% power conversion efficiency*. ACS Energy Letters, 2019. **4**(6): p. 1258-1259.
70. Jiang, Q., et al., *Surface passivation of perovskite film for efficient solar cells*. Nature Photonics, 2019. **13**(7): p. 460-466.
71. Hu, M., et al., *Sub-1.4 eV bandgap inorganic perovskite solar cells with long-term stability*. Nature Communications, 2020. **11**(1): p. 1-10.
72. Babaei, A., et al., *Efficient vacuum deposited pin perovskite solar cells by front contact optimization*. Frontiers in Chemistry, 2020. **7**: p. 936.
73. Green, M.A., et al., *Solar cell efficiency tables (version 52)*. Progress in Photovoltaics: Research and Applications, 2018. **26**(7): p. 427-436.
74. Jeon, N.J., et al., *o-Methoxy substituents in spiro-OMeTAD for efficient inorganic-organic hybrid perovskite solar cells*. Journal of the American Chemical Society, 2014. **136**(22): p. 7837-7840.
75. Chen, W., et al., *Efficient and stable large-area perovskite solar cells with inorganic charge extraction layers*. Science, 2015. **350**(6263): p. 944-948.

76. Tyona, M., *A theoretical study on spin coating technique*. Advances in materials Research, 2013. **2**(4): p. 195.
77. Yilbas, B.S., A. Al-Sharafi, and H. Ali, *Self-Cleaning of Surfaces and Water Droplet Mobility*. 2019: Elsevier.
78. Wasa, K., I. Kanno, and H. Kotera, *Handbook of sputter deposition technology: fundamentals and applications for functional thin films, nano-materials and MEMS*. 2012: William Andrew.
79. Birkholz, M., *Thin film analysis by X-ray scattering*. 2006: John Wiley & Sons.
80. Cullity, B.D. and S.R. Stock, *Elements of X-ray Diffraction*. Vol. 3. 2001: Prentice hall New Jersey.
81. Uvarov, V. and I. Popov, *Metrological characterization of X-ray diffraction methods for determination of crystallite size in nano-scale materials*. Materials characterization, 2007. **58**(10): p. 883-891.
82. Pielaszek, R., *Diffraction studies of microstructure of nanocrystals exposed to high pressure*. 2003, Ph. D. thesis, Warsaw University, Department of Physics, Warsaw, Poland.
83. Baskaran, S., *Structure and regulation of yeast glycogen synthase*. 2010.
84. Akhtar, K., et al., *Scanning Electron Microscopy: Principle and Applications in Nanomaterials Characterization*, in *Handbook of Materials Characterization*. 2018, Springer. p. 113-145.
85. Girão, A.V., G. Caputo, and M.C. Ferro, *Application of Scanning Electron Microscopy–Energy Dispersive X-Ray Spectroscopy (SEM-EDS)*, in *Comprehensive Analytical Chemistry*. 2017, Elsevier. p. 153-168.
86. Inkson, B., *Scanning electron microscopy (SEM) and transmission electron microscopy (TEM) for materials characterization*, in *Materials characterization using nondestructive evaluation (NDE) methods*. 2016, Elsevier. p. 17-43.
87. Alyamani, A. and O. Lemine, *FE-SEM characterization of some nanomaterial*, in *Scanning electron microscopy*. 2012, IntechOpen.
88. Mishra, R.K., A.K. Zachariah, and S. Thomas, *Energy-Dispersive X-ray Spectroscopy Techniques for Nanomaterial*, in *Microscopy Methods in Nanomaterials Characterization*. 2017, Elsevier. p. 383-405.
89. Workman Jr, J. and A. Springsteen, *Applied spectroscopy: a compact reference for practitioners*. 1998: Academic Press.
90. Rocha, F.S., et al., *Experimental methods in chemical engineering: Ultraviolet visible spectroscopy—UV-Vis*. The Canadian Journal of Chemical Engineering, 2018. **96**(12): p. 2512-2517.

91. Perkampus, H.-H., *UV-VIS Spectroscopy and its Applications*. 2013: Springer Science & Business Media.
92. Viezbicke, B.D., et al., *Evaluation of the Tauc method for optical absorption edge determination: ZnO thin films as a model system*. *physica status solidi (b)*, 2015. **252**(8): p. 1700-1710.
93. Hossain, S., *Performance and stability of perovskite solar cells*. 2018.
94. da Silva Filho, J.M.C., V.A. Ermakov, and F.C. Marques, *Perovskite thin film synthesised from sputtered lead sulphide*. *Scientific reports*, 2018. **8**(1): p. 1-8.
95. Gujar, T.P., et al., *The role of Pbl 2 in CH 3 NH 3 Pbl 3 perovskite stability, solar cell parameters and device degradation*. *Physical Chemistry Chemical Physics*, 2018. **20**(1): p. 605-614.
96. Chen, L., et al., *Efficient air-stable perovskite solar cells with a (FAI) 0.46 (MAI) 0.40 (MABr) 0.14 (Pbl 2) 0.86 (PbBr 2) 0.14 active layer fabricated via a vacuum flash-assisted method under RH> 50%*. *RSC Advances*, 2019. **9**(18): p. 10148-10154.
97. Saliba, M., et al., *Perovskite solar cells: from the atomic level to film quality and device performance*. *Angewandte Chemie International Edition*, 2018. **57**(10): p. 2554-2569.